Nano Research

ISSN 1998-0124 CN 11-5974/O4
https://doi.org/10.26599/NR.2026.94909295

Research Article

MXene@C/SiO_2 composite films with layered heterostructures for high-temperature infrared stealth, electromagnetic interference shielding, and fire safety

Nan Pang[1,2], Xiaoqing Yin[1,2], Yi Lu[3], Xiao Cheng[1](✉), Meijie Yu[1,2](✉)

[1] State Key Laboratory of Coatings for Advanced Equipment, School of Materials Science & Engineering, Shandong University, Jinan 250061, China

[2] Shandong Key Laboratory of Carbon Fiber and Composite Materials Manufacture and Application, Weihai 264211, China

[3] Shandong Institute of Nonmetallic Materials, Jinan 250031, China

Nano Res., **Just Accepted Manuscript** • https://doi.org/10.26599/NR.2026.94909295

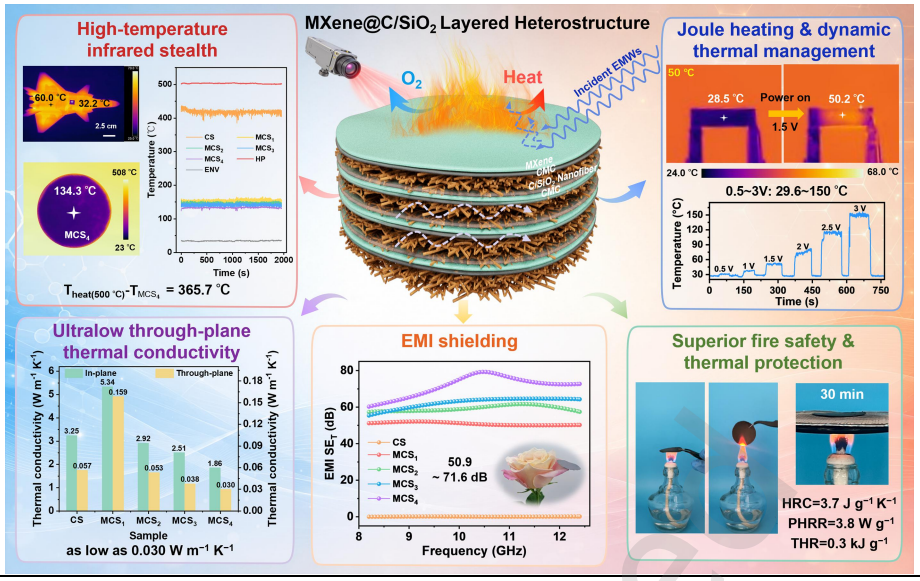
https://www.sciopen.com/journal/1998-0124 on Oct. 28, 2026

© The Authors(s)

Just Accepted

This is a "Just Accepted" manuscript, which has been examined by the peer-review process and has been accepted for publication. A "Just Accepted" manuscript is published online shortly after its acceptance,which is prior to technical editing and formatting and author proofing. Tsinghua University Press (TUP) provides "Just Accepted" as an optional and free service which allows authors to make their results available to the research community as soon as possible after acceptance. After a manuscript has been technically edited and formatted, and the page proofs have been corrected, it will be removed from the "Just Accepted" web site and published officially with volume and article number (e.g., *Nano Research*, **2025**, *18*, 94906990). Please note that technical editing may introduce minor changes to the manuscript text and/or graphics which may affect the content, and all legal disclaimers that apply to the journal pertain. In no event shall TUP be held responsible for errors or consequences arising from the use of any information contained in these "Just Accepted" manuscripts. To cite this anuscript please use its Digital Object Identifier (DOI®),which is identical for all formats of publication.

Just Accepted



Layered MXene@C/SiO_2 composite films with tunable heterogeneous architectures integrate high-temperature infrared stealth, ultralow through-plane thermal conductivity, efficient Joule heating, strong EMI shielding, and fire safety. The synergistic regulation of thermal transport, infrared radiation, and electromagnetic attenuation provides a promising strategy for flexible multifunctional protective materials.

Just Accepted

Nano Research

Open Access

Research Article

MXene@C/SiO_2 composite films with layered heterostructures for high-temperature infrared stealth, electromagnetic interference shielding, and fire safety

Nan Pang[1,2], Xiaoqing Yin[1,2], Yi Lu[3], Xiao Cheng[1] ✉, Meijie Yu[1,2] ✉

[1] *State Key Laboratory of Coatings for Advanced Equipment, School of Materials Science & Engineering, Shandong University, Jinan 250061, China*
[2] *Shandong Key Laboratory of Carbon Fiber and Composite Materials Manufacture and Application, Weihai 264211, China*
[3] *Shandong Institute of Nonmetallic Materials, Jinan 250031, China*

Received: 2 September 2026; **Revised:** 10 October 2026; **Accepted:** 28 October 2026

✉ Address correspondence to Meijie Yu, yumeijie@sdu.edu.cn; Xiao Cheng, chengxiao@sdu.edu.cn

Cite this article: *Nano Research*, 2026, 19, 94909295 https://doi.org/10.26599/NR.2026.94909295

ABSTRACT: Flexible materials integrating infrared stealth, electromagnetic interference (EMI) shielding, thermal management, and fire safety are highly desirable for aerospace and high-temperature electronics. Here, layered MXene@C/SiO_2 composite films (MCS_x) with tunable structural units were constructed by combining low-thermal-conductivity C/SiO_2 nanofiber layers with highly conductive MXene layers. This heterogeneous architecture endows the films with pronounced anisotropic thermal transport and an ultralow through-plane thermal conductivity of 0.030 W m^{-1} K^{-1}. Benefiting from the low emissivity of MXene and efficient thermal insulation, the films achieve infrared stealth over 50–500 °C and reduce the apparent surface temperature by 365.7 °C at a heat source temperature of 500 °C. The continuous MXene network enables rapid Joule heating from 29.5 to 149.6 °C at 0.5–3.0 V with an electrothermal conversion efficiency exceeding 99%. The conductive layers and heterogeneous interfaces jointly achieve an X-band EMI shielding effectiveness of 71.6 dB. The films also exhibit excellent flame retardancy, thermal insulation, and fire resistance while maintaining EMI shielding performance after flame exposure. This work provides a heterostructure engineering strategy for developing multifunctional protective materials under thermally demanding conditions.

KEYWORDS: $Ti_3C_2T_x$ MXene, C/SiO_2 nanofibers, infrared stealth, electromagnetic interference shielding, flame retardancy

Just Accepted

1 Introduction

With the rapid development of multispectral detection technologies, high-resolution infrared imaging systems, and sophisticated electromagnetic countermeasure technologies, advanced aerospace systems, wearable systems, flexible electronics, and stealth platforms are facing increasingly demanding service environments. During operation, these systems continuously emit detectable infrared radiation while facing complex electromagnetic interference, high-temperature heat fluxes, and potential fire hazards [1-5]. Therefore, lightweight, flexible materials integrating infrared (IR) stealth, electromagnetic interference (EMI) shielding, thermal management, flame retardancy, and thermal insulation are increasingly important for advanced protection.

IR stealth and EMI shielding are two key performance requirements for advanced protective materials. IR stealth reduces the radiation contrast between a target and its surroundings by lowering surface emissivity and suppressing the surface-temperature rise [6], whereas efficient EMI shielding relies on the reflection, absorption, and dissipation of incident electromagnetic waves [7]. Recent studies have demonstrated that, compared with relying solely on low emissivity, the heterogeneous integration of a low-emissivity functional layer with a low-thermal-conductivity insulating layer enables simultaneous regulation of surface radiation characteristics and heat transport behavior [8-10]. Suppressing heat transfer from a heat source to the outer surface improves high-temperature stealth, thermal protection, and operational safety. Meanwhile, abundant interfaces promote interfacial polarization and enhance electromagnetic-wave attenuation, increasing electromagnetic energy dissipation [11, 12]. Layered heterostructures are thus promising for integrating radiative regulation, thermal insulation, and electromagnetic attenuation.

Among the various candidate materials, $Ti_3C_2T_x$ MXene has attracted considerable attention for EMI shielding, Joule heating, and infrared regulation owing to its excellent electrical conductivity, abundant surface functional groups, and solution processability [13, 14]. Conductive MXene layers reflect electromagnetic waves and enable rapid electrothermal conversion, while their intrinsically low infrared emissivity suppresses thermal radiation. However, low emissivity alone is insufficient for high-temperature infrared stealth, and integrating it with efficient thermal insulation remains a key challenge. To address this issue, MXene has been integrated with polymers, aerogels, and inorganic fibers to reduce thermal conductivity and improve thermal protection [2, 9, 15]. However, polymer matrices remain susceptible to thermal degradation at elevated temperatures, limiting their fire resistance. Aerogels generally require relatively large thicknesses to achieve effective thermal insulation. In contrast, inorganic nanofiber films combine low density and intrinsically low thermal conductivity, making them

promising candidates for high-performance thermal protection systems [16-18]. Among the various fabrication techniques, electrospinning has been widely adopted for producing flexible inorganic nanofiber films because of its simplicity, low cost, and excellent structural tunability. However, conventional inorganic nanofiber films tend to become brittle after high-temperature processing, resulting in reduced flexibility and structural stability, which restricts their practical applications [19, 20].

Inspired by these considerations, a layered MXene@C/SiO_2 heterostructure with tunable structural units was constructed. Poly(vinyl alcohol) (PVA)/SiO_2 nanofiber films were fabricated by combining in situ hydrolysis of tetraethyl orthosilicate (TEOS) with electrospinning, and the effects of different carbonization temperatures on the dimensional stability and flexibility of the resulting C/SiO_2 fibrous films were systematically investigated to obtain a C/SiO_2 nanofibrous framework with good structural integrity and flexibility. Subsequently, low-emissivity MXene layers and low-thermal-conductivity C/SiO_2 nanofibrous layers were alternately assembled using sodium carboxymethyl cellulose (CMC-Na) as an interfacial binder, forming a layered heterostructure with abundant interfaces and high interfacial thermal resistance. By varying the number of MXene@C/SiO_2 structural units, the heterogeneous interfaces and interfacial thermal resistance can be systematically regulated. The alternating architecture combines the low emissivity and high conductivity of MXene with the low thermal conductivity and thermal stability of C/SiO_2 nanofiber layers, enabling coordinated regulation of infrared radiation, heat transport, and electromagnetic response. This work reveals the synergistic role of low emissivity, anisotropic heat transport, and interfacial thermal resistance in high-temperature infrared stealth, and provides a tunable heterostructure strategy for integrating infrared stealth, EMI shielding, thermal management, and fire protection.

2 Experimental

2.1 Materials

Titanium aluminum carbide (Ti_3AlC_2, 99%, 400 mesh) was purchased from Jilin Yiyi Technology Co., Ltd. Tetraethyl orthosilicate (TEOS, 98%) was purchased from Macklin Biochemical Co., Ltd. Hydrochloric acid (HCl, 36–38 wt%) was obtained from Sinopharm Chemical Reagent Co., Ltd. Sodium carboxymethyl cellulose (CMC-Na, viscosity 800–1200 mPa·s) was purchased from Shanghai Yuanye Bio-Technology Co., Ltd. Lithium fluoride (LiF, 99.9%), poly(vinyl alcohol) (PVA, degree of alcoholysis 88%), and oxalic acid ($H_2C_2O_4$, 99%) were obtained from Shanghai Aladdin Biochemical Technology Co., Ltd. Deionized water prepared in-house was used throughout the experiments. All chemicals were used as received without further purification.

2.2 Preparation of $Ti_3C_2T_x$ MXene films

A $Ti_3C_2T_x$ colloidal suspension was prepared by in situ etching. LiF (3.2 g) was dissolved in HCl (40 mL, 9 mol L^{-1}), and Ti_3AlC_2 powder (2 g) was gradually added under stirring. The mixture was held at 40 °C for 30 h to remove the Al layers and centrifugally washed with deionized water until the supernatant reached near-neutral pH. Few-/single-layer $Ti_3C_2T_x$ nanosheets were obtained by ultrasonication and gradient centrifugation. The dispersion was freeze-dried at −55 °C for 24 h and redispersed in deionized water at 40 mg mL^{-1}. To facilitate large-area fabrication, the suspension was blade-coated onto polyethylene terephthalate substrates. After drying, the MXene films were cut to the required dimensions.

2.3 Preparation of C/SiO_2 nanofiber films

PVA (12 g) was dispersed in deionized water (88 g), swollen at room temperature for 30 min, and stirred at 80 °C for 4 h to form a 12 wt% solution. A TEOS hydrolysate containing TEOS, H_2O, and $H_2C_2O_4$ (molar ratio 1:8.063:0.0186) was magnetically stirred for 9 h until clear. The PVA solution and TEOS hydrolysate were mixed at a mass ratio of 6:4 and stirred for 3.5 h. After vacuum degassing, the precursor was electrospun at 12–18 kV, with a feed rate of 0.04–0.08 mm min^{-1}, a drum speed of 450 rpm, a tip-to-collector distance of 20–25 cm, an ambient temperature of 20–25 °C, and a relative humidity of 30%–40%. PVA/SiO_2 films were dried at 60 °C for 24 h, heated to 240 °C at 1 °C min^{-1}, and pre-oxidized for 2 h. The pre-oxidized films were placed between two alumina ceramic plates and carbonized under an Ar atmosphere. They were heated to 300 °C at 2 °C min^{-1} for 1 h and then to 550 °C at 1.5 °C min^{-1} for another 1 h. This sample was designated the 550 °C-carbonized film. Selected samples were further heated to 650, 700, or 800 °C at 2 °C min^{-1} and held for 2 h. The films were furnace-cooled below 60 °C. Unless otherwise stated, CS denotes the film carbonized at 650 °C.

2.4 Preparation of MXene@C/SiO_2 composite films

A 4 wt% adhesive was prepared by gradually dissolving 2 g of CMC-Na in 48 g of deionized water under continuous stirring at 60 °C. MXene and C/SiO_2 films with a diameter of 40 mm were alternately stacked using CMC-Na as the interfacial adhesive. For each interface, approximately 2 mL of CMC-Na solution was uniformly applied by brush-coating. The films were then subjected to a load of 9.8 N for 20 min to ensure intimate interfacial contact while minimizing excessive infiltration of the adhesive into the porous fibrous layers. The assembled laminates were subsequently vacuum-dried at 40 °C for 4 h. Films containing one to four MXene@C/SiO_2 structural units were denoted MCS_x (x = 1, 2, 3, and 4).

2.5 Characterization

Surface and cross-sectional morphologies were examined using a field-emission scanning electron microscope (SEM, Hitachi SU-70). Morphology and crystal structure were characterized using transmission electron microscopy (TEM, JEOL JEM-F200). Crystal structures were analyzed by X-ray diffraction (XRD, SmartLab, 9 kW). Fourier transform infrared spectroscopy (FTIR, Bruker Tensor II) was employed to identify functional groups, while elemental composition and chemical states were investigated using X-ray photoelectron spectroscopy (XPS, Thermo Scientific ESCALAB Xi+). Infrared emissivity in the 8–14 μm atmospheric window was measured using a dual-band infrared emissometer (IR-II). Infrared apparent temperatures and temperature distributions were recorded using a thermal imaging camera (Fluke RSE30) under identical measurement conditions and analyzed using SmartView IR software, while actual surface temperatures were independently measured using a thermocouple. Thermal diffusivity and conductivity were measured using a laser flash analyzer (LFA 467, NETZSCH). Electrical conductivity was determined using a four-point probe system (RTS-9). Thermogravimetric analysis (TGA, NETZSCH TG 209 F1) was conducted under N_2 at 10 °C min^{-1}, with MXene additionally tested in air. Limiting oxygen

Just Accepted

index (LOI) was measured using an FTT0077 oxygen index analyzer according to GB/T 2406. Heat release capacity (HRC), peak heat release rate (PHRR), and total heat release (THR) were determined using a microscale combustion calorimeter (MCC, DEATAK MCC-3). Joule heating performance was evaluated using a DC regulated power supply (WPS3010B). Electromagnetic interference (EMI) shielding performance of the films in the X-band (8.2–12.4 GHz) was measured using a vector network analyzer (Agilent N5244A PNA-X).

3 Results and Discussion

3.1 Morphological and structural characterization of C/SiO_2 nanofiber films and MCS_x composite films

The morphology and structural characterization shown in Supplementary Figs. S1(a)–(c) in the Electronic Supplementary Material (ESM) confirm the successful synthesis of $Ti_3C_2T_x$ MXene, consistent with previous reports [15, 21, 22]. As illustrated in Fig. 1(a), PVA/SiO_2 nanofiber films were first prepared by electrospinning. Pre-oxidation and stepwise carbonization converted them into flexible C/SiO_2 nanofiber films. These films were then alternately assembled with MXene using CMC-Na as an interfacial binder to produce layered MCS_x films with different numbers of structural units. The as-spun, pre-oxidized, and 650 °C-carbonized films retain intact three-dimensional interconnected fibrous networks (Figs. 1(b)–1(b_2)); morphologies at other carbonization temperatures are shown in Fig. S2 in the ESM. Pre-oxidation decreases the mean fiber diameter from approximately 1.5 μm to 899.3 nm through dehydration, polymer-chain rearrangement, and densification of the PVA matrix [23]. Continuous pyrolysis and carbon-framework shrinkage further decrease the diameter from 791.4 nm at 550 °C to 748.5 nm at 700 °C. At 800 °C, it increases slightly to 780.0 nm because of SiO_2-network reconstruction and localized fiber fusion [24]. Consistently, the film area shrinkage increases with carbonization temperature (Fig. S3 in the ESM). Uniform C, Si, and O distributions throughout the network confirm formation of a homogeneous C/SiO_2 composite

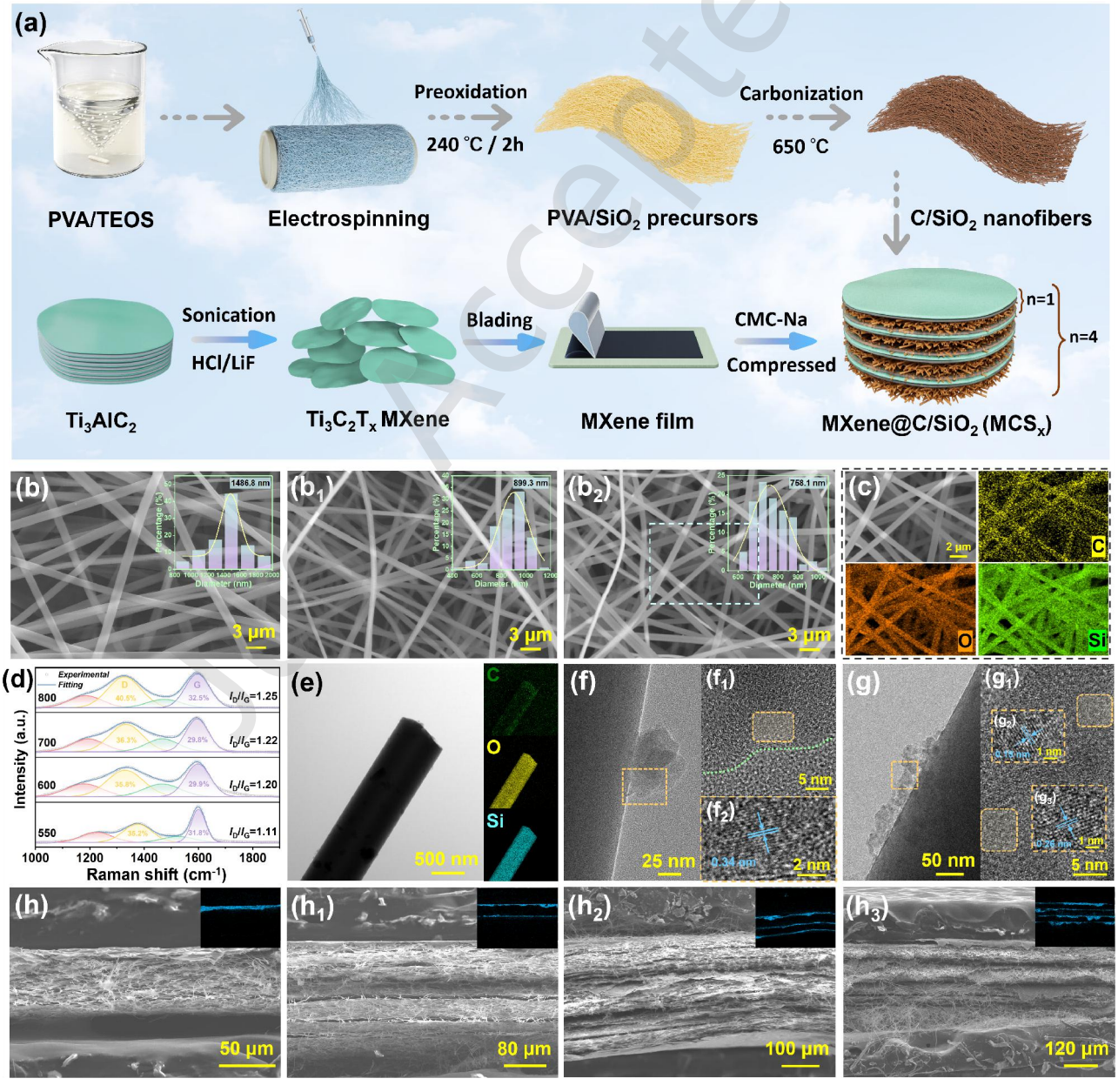


Figure 1 (a) Schematic illustration of the fabrication process of the MCS_x composite films. SEM images and diameter distributions of (b) as-spun, (b_1) pre-

oxidized, and (b_2) 650 °C-carbonized nanofibers. (c) Enlarged SEM image of the region marked in (b_2) and the corresponding EDS elemental mapping. (d) Raman spectra at different carbonization temperatures. (e) TEM image of a single C/SiO_2 nanofiber and the corresponding elemental mapping. (f–f_2, g–g_3) Magnified TEM images showing local graphitic domains. (h–h_3) Cross-sectional SEM images and Ti maps of MCS_1–MCS_4.

framework (Fig. 1(c)).

All films exhibit D and G bands corresponding to disordered and sp^2-hybridized graphitic carbon, respectively (Fig. 1(d)) [25, 26]. The D band shifts from approximately1377 cm^{-1} at 550 °C to 1332 cm^{-1} at 650–800 °C, indicating a considerable amount of incompletely aromatized carbon at 550 °C. With increasing temperature, sp^2 clusters develop toward a turbostratic graphite structure. The I_D/I_G ratio consequently increases from 1.11 to 1.25 as small sp^2 carbon nanocrystallites and edge-defect sites form [27-29]. Nearly identical spectra at 650 and 700 °C indicate that the carbon structure is essentially established at 650 °C. Higher temperatures provide little additional ordering but cause greater macroscopic shrinkage and morphological change; therefore, the 650 °C film was selected for subsequent tests.

TEM imaging and elemental mapping of a single C/SiO_2 fiber are consistent with the SEM-EDS results (Fig. 1(e)). Ultrasonication during TEM sample preparation induced partial delamination of the fiber surface, generating thin flake-like fragments that facilitated direct observation of the internal structure. High-resolution images show a predominantly amorphous structure containing only localized, short-range ordered, discontinuous lattice fringes (Figs. 1(f)–1(g_3)). Spacings of 0.34, 0.26, and 0.19 nm are assigned to the (002), (102), and (100) planes of turbostratic graphitic carbon nanocrystallites, respectively [29-31]. Thus, carbonization at 650 °C produces partially graphitized microcrystalline domains, whereas the absence of crystalline SiO_2 fringes indicates that SiO_2 remains amorphous. Cross-sectional images and Ti elemental mapping confirm that MXene and C/SiO_2 fibrous layers are alternately stacked into a well-defined heterostructure in MCS_1–MCS_4 (Figs. 1(h)–1(h_3)). The surface MXene layer exhibits dense lamellar stacking and a typical wrinkled morphology (Figs. 2(a) and 2(b). Photographs at different fabrication stages are shown in Fig. 2(c). The completed film can be supported by a single flower petal, demonstrating its lightweight character (Fig. 2(d)).

XRD was used to examine phase composition and structural evolution. As the number of units increases, the MXene (002) peak shifts to lower angles and develops a weak shoulder, indicating expanded interlayer spacing (Fig. 2(e)). This evolution is attributed to CMC-Na shrinkage during drying and constraint from the C/SiO_2 nanofiber film, which introduce out-of-plane tensile stress into the MXene layers. The rough fibrous surface also wrinkles the MXene nanosheets and reduces local stacking order [32, 33]. With further stacking, accumulated orientation mismatch and local stress perturbations among adjacent MXene layers cause peak broadening and shoulder formation [34]. Because the C/SiO_2 film contains mainly amorphous carbon and SiO_2, its diffraction features are broad and weak. The absence of crystalline SiO_2 peaks agrees with the TEM observations. The low-angle shift and peak broadening indicate increased interlayer spacing and stacking disorder, consistent with partial insertion of CMC-Na chains into the MXene interlayers and physical confinement from adjacent C/SiO_2 nanofiber layers.

The FTIR spectra show a broad –OH stretching band at approximately 3430 cm^{-1}, arising from surface silanol groups, CMC-Na hydroxyl groups, MXene terminal –OH groups, and adsorbed water (Fig. 2(f)). The bands at 1080, 800, and 460 cm^{-1} correspond to the asymmetric stretching, symmetric stretching, and bending vibrations of Si–O–Si, respectively, confirming formation of a continuous SiO_2 network [35, 36]. Bands at 500–700 cm^{-1} are assigned mainly to Ti–O, Ti–O–Ti, and Ti–C

Just Accepted

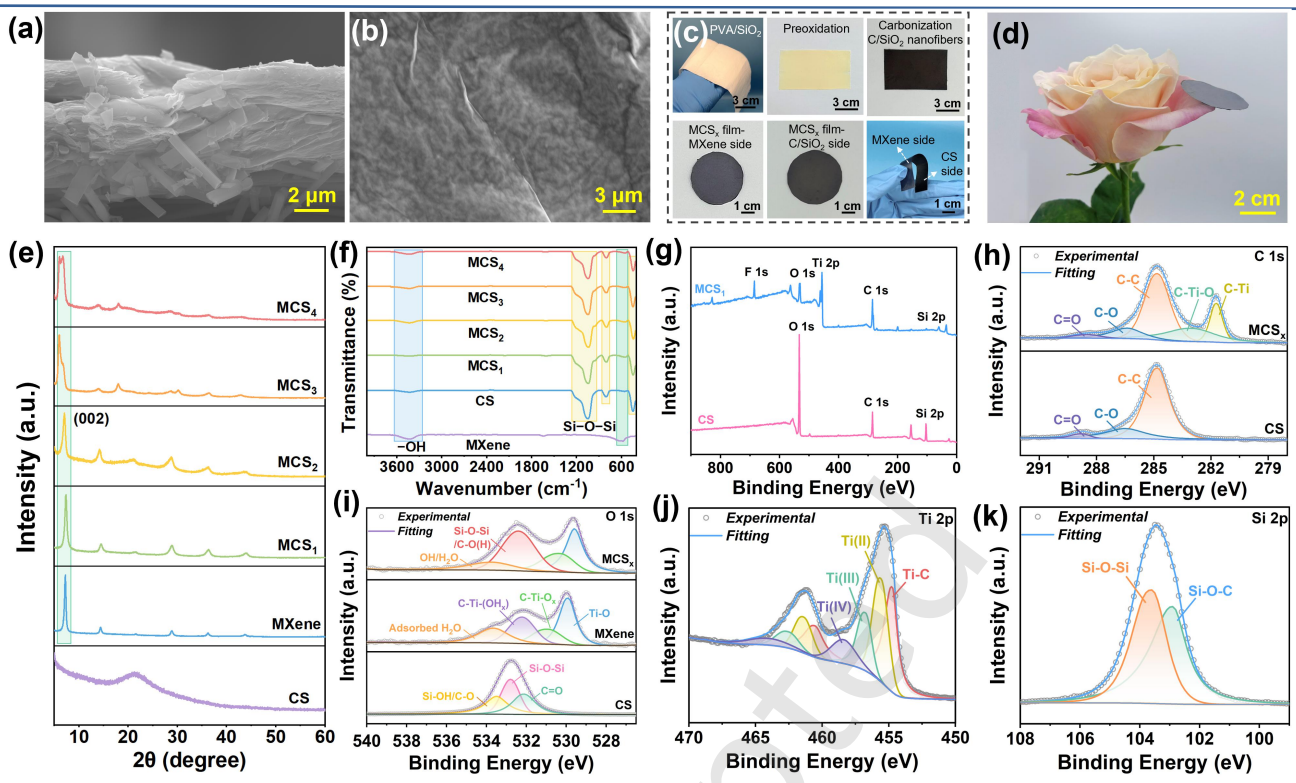


Figure 2 (a) Cross-sectional SEM image of the surface layer of the composite film. (b) Surface morphology of the composite film. (c) Fabrication-stage photographs and (d) lightweight demonstration. (e) XRD patterns and (f) FTIR spectra of the composite films. (g) XPS survey spectra of CS and MCS_x films. (h) High-resolution C 1s XPS spectra of CS and MCS_x. (i) High-resolution O 1s XPS spectra of CS, pristine MXene, and MCS_x. High-resolution XPS spectra of MCS_x films: (j) Ti 2p and (k) Si 2p.

vibrations in MXene [37, 38]. Their unchanged positions from MCS_1 to MCS_4 indicate that assembly causes no substantial chemical transformation. Meanwhile, the abundant hydroxyl-containing groups provide possible interaction sites for CMC-Na-mediated interfacial adhesion.

XPS was further used to analyze elemental composition and chemical states. The survey spectra show Ti together with C, O, and Si in MCS_x, confirming successful MXene incorporation (Fig. 2(g)). The C 1s peaks of CS at 284.8, 286.5, and 288.8 eV correspond to C–C, C–O, and C=O bonds, respectively (Fig. 2(h)). Two additional MCS_x peaks at 281.7 and 283.1 eV arise from the characteristic C–Ti and C–Ti–O configurations of MXene (Fig. 2(h)) [39]. High-resolution O 1s XPS spectra were further analyzed to probe changes in the interfacial chemical environment. As shown in Fig. 2(i), after assembly, MCS_x exhibits oxygen-related contributions from both CS and pristine MXene, while the Ti–O and C–Ti–O_x components show slight binding-energy shifts (from 529.9 to 529.6 eV and from 530.9 to 530.3 eV, respectively). These changes indicate a modified local electronic environment of oxygen-containing species after assembly. The Ti 2p components at 454.8, 455.7, 456.8, and 458.5 eV are assigned to Ti–C, Ti^{2+}, Ti^{3+}, and Ti^{4+}, respectively (Fig. 2(j)) [21]. The Si 2p peaks at 102.9 and 103.7 eV correspond to Si–O–C and Si–O–Si bonds (Fig. 2(k)) [40]. Together with the FTIR and XRD results, the XPS analysis indicates that the interfacial bonding in the MCS_x composite films is mainly governed by CMC-Na-mediated physical adhesion involving hydrogen bonding and polar interactions, rather than the formation of new strong covalent bonds.

3.2 Infrared stealth performance and anisotropic thermal conductivity

Infrared stealth requires minimal radiation contrast between a target and its surroundings. The 8–14 μm band is a major long-wave infrared atmospheric window with relatively high atmospheric transmittance and is widely used for thermal imaging and infrared detection. According to the Stefan–Boltzmann law ($E = \varepsilon\sigma T^4$) [6], radiation intensity depends jointly on emissivity (ε) and actual temperature (T). Simultaneous regulation of emissivity and heat transfer can therefore suppress the infrared signature within this atmospheric window more effectively than either strategy alone. Here, the infrared stealth performance of the films was systematically evaluated over a temperature range of 30-500 °C.

As the number of structural units increases from 1 to 4, the film thickness increases from 0.075 to 0.26 mm (Fig. 3(a)), while the electrical conductivity decreases from 200 to 60 S cm^{-1} (Fig. 3(b)) and the average infrared emissivity increases (Fig. 3(c)). On the one hand, the increased number of structural units introduces more heterogeneous interfaces and contact resistance, thereby weakening continuous charge-carrier transport. According to the Hagen–Rubens relation, the resulting decrease in conductivity reduces infrared reflectivity and thus increases emissivity [41]. Meanwhile, the denser interfaces promote multiple reflections, scattering, and absorption of infrared radiation. According to Kirchhoff's law, the enhanced absorptivity further increases infrared emissivity [13]. Increasing interface density therefore affects both electrical transport and the radiative response of multilayer films.

Practical infrared stealth was evaluated on a temperature-gradient platform from 50 to 500 °C at 50 °C intervals. The apparent temperatures of the heat source (HS), MCS_x film, and environment (ENV) were monitored using an infrared camera.

In Accepted

The measurements directly capture both heat-source suppression and environmental contrast, allowing the influence of structural-unit number on the apparent infrared signature to be assessed across the full temperature range. As shown in Fig. 3(d) and Fig. S4 in the ESM, the apparent surface temperature decreases as the number of structural units increases, confirming improved infrared stealth. Fig. 3(e) and Table S1 in the ESM summarize the apparent temperature difference (ΔT) between the film and heat source. MCS_1 reduces the apparent temperature by 21.4–344.4 °C, whereas MCS_4 achieves reductions of 23.6–365.7 °C. The films also demonstrate infrared stealth on human skin, high-temperature aircraft models, and low-temperature targets (Figs. 3(f)–3(i)). Figs. 4(a)–4(e) and Fig. S5 in the ESM present the temperature response curves of different samples under continuous thermal shock. During continuous heating for more than 30 min, the surface temperatures of all samples remained stable, demonstrating good thermal stability under the present test conditions. Compared with previously reported MXene-based infrared stealth materials (Fig. 4(f) and Table S2 in the ESM), the layered heterostructure developed in this work demonstrates superior high-temperature infrared stealth performance.

The anisotropic thermal transport behavior of the composite films was investigated to clarify the infrared stealth mechanism. As shown in Fig. 4(g) and Tables S3 and S4 in the ESM, the in-plane thermal conductivities of the CS, MCS_1, MCS_2, MCS_3, and MCS_4 films are 3.248, 5.340, 2.920, 2.514, and 1.858 W m^{-1} K^{-1}, respectively, while the corresponding through-plane thermal conductivities are 0.057, 0.159, 0.053, 0.038, and 0.030 W m^{-1} K^{-1}. Both conductivities decrease with increasing structural units. Notably, the through-plane thermal conductivity of MCS_4 is as low as 0.030 W m^{-1} K^{-1}, surpassing that of many conventional thermal insulation materials. The pronounced thermal transport anisotropy originates from the synergistic regulation of the layered heterostructure. On the one hand, the C/SiO_2 nanofiber network and the abundant inter-fiber air voids enhance phonon scattering, thereby suppressing phonon-mediated heat transport. On the other hand, the highly aligned MXene layers provide relatively continuous in-plane pathways for heat transport, whereas the weak interlayer interactions effectively suppress through-plane heat transport. Moreover, the multiple MXene@C/SiO_2 heterogeneous interfaces and CMC-Na interlayers introduce substantial interfacial thermal resistance, further impeding phonon transport across adjacent layers. Consequently, heat preferentially propagates laterally along the MXene layers, whereas through-plane heat transport is effectively suppressed, as schematically illustrated in Fig. 4(h). Together with the intrinsically low infrared emissivity of MXene, this anisotropic thermal transport behavior synergistically suppresses infrared radiation, thereby enhancing the infrared stealth performance of the composite films.

Notably, although MCS_4 exhibits a slightly higher average infrared emissivity (0.216) than MCS_1 (0.142), it demonstrates superior infrared stealth performance. In particular, under a 500 °C heat source, the apparent surface temperature of MCS_4 (134.3 °C) is substantially lower than that of MCS_1 (155.6 °C), corresponding to an approximately 6.2% greater apparent temperature reduction. Moreover, when the heating stage is maintained at 500 °C, thermocouple measurements indicate that

Just Accepted

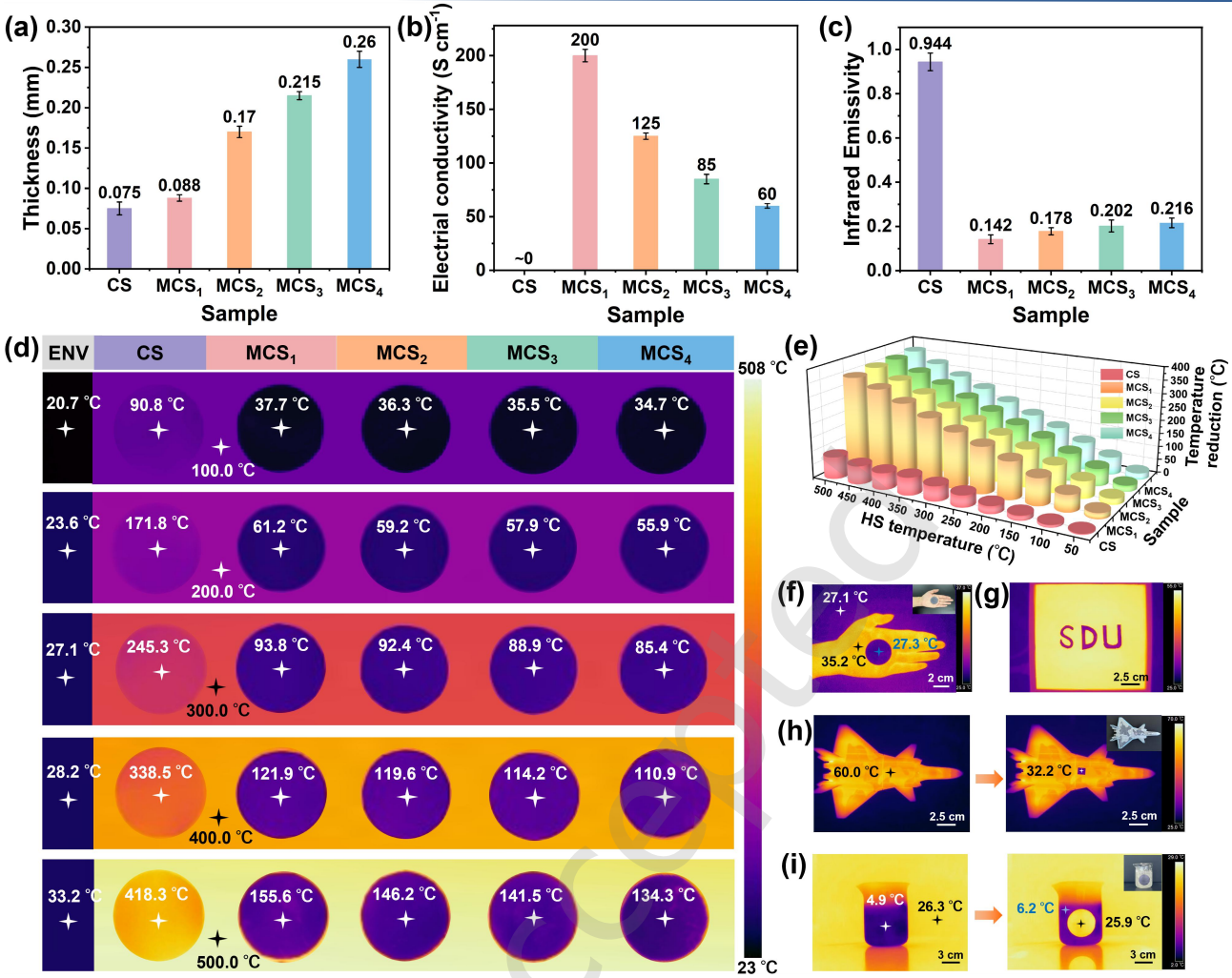


Figure 3 (a) Thickness, (b) electrical conductivity, and (c) 8–14 μm emissivity of MCS_x composite films. (d) Infrared images and (e) apparent temperature reductions at different heat-source temperatures. Demonstrations of infrared stealth performance for the composite film: (f) on a human palm, (g) infrared signal transmission test, (h) on an aircraft model, and (i) on a low-temperature target.

the actual surface temperatures of the MCS_1 and MCS_4 films are approximately 468 and 415 °C, respectively. According to Planck's law of thermal radiation, the integrated infrared radiation intensity within the 8–14 μm atmospheric window is calculated according to Eq. (1) in the ESM. Quantitative analysis reveals that the theoretical contributions of low emissivity and thermal insulation to infrared signal suppression are 93.6% and 6.4%, respectively, for MCS_1, whereas the corresponding values for MCS_4 are 81.1% and 18.9%, respectively. These results provide quantitative evidence for the synergistic contributions of low emissivity and thermal insulation to infrared radiation regulation. Despite its slightly higher average emissivity, MCS_4 possesses a lower through-plane thermal conductivity and a higher thermal resistance owing to its layered heterostructure, leading to a substantially reduced actual surface temperature. Consequently, the integrated thermal radiation emitted within the 8–14 μm atmospheric window is effectively suppressed, offsetting the adverse effect of the slightly increased emissivity and ultimately resulting in a lower infrared radiation intensity and superior high-temperature infrared stealth performance.

3.3 Joule heating performance and dynamic thermal management applications

Enabled by the construction of a continuous MXene conductive network, the MCS_x composite films exhibit excellent Joule heating performance. As shown in Fig. 5(a), the film rapidly reaches thermal equilibrium under input voltages of 0.5, 1.0, 1.5, 2.0, 2.5, and 3.0 V, reaching steady-state temperatures of 29.5, 39.6, 57.9, 83.4, 114.2, and 149.6 °C, respectively. After the power is switched off, the temperature rapidly returns to ambient temperature, demonstrating fast and reversible electrothermal behavior. Continuous voltage ramping and cycling tests (Fig. 5(b)) further show that the surface temperature can be stably regulated over a wide range of 29.5–149.6 °C, demonstrating precise temperature control.

Infrared thermal images at different input voltages are shown in Fig. 5(c). A uniform temperature distribution is observed across the film surface during electrical heating without noticeable local hot spots, indicating the formation of a homogeneous and continuous conductive network throughout the composite. To evaluate the operational stability, 30 consecutive on/off heating cycles are performed at 2 V (Fig. 5(d)). The heating curves almost completely overlap without performance degradation, confirming the film's outstanding cycling stability and electrothermal reliability. To evaluate electrothermal conversion, the electrothermal conversion efficiency (η) was calculated according to Eq. (2) in the ESM [6].

As shown in Fig. 5(e), the efficiency remains at a high level throughout the applied voltage range of 0.5–3.0 V, indicating

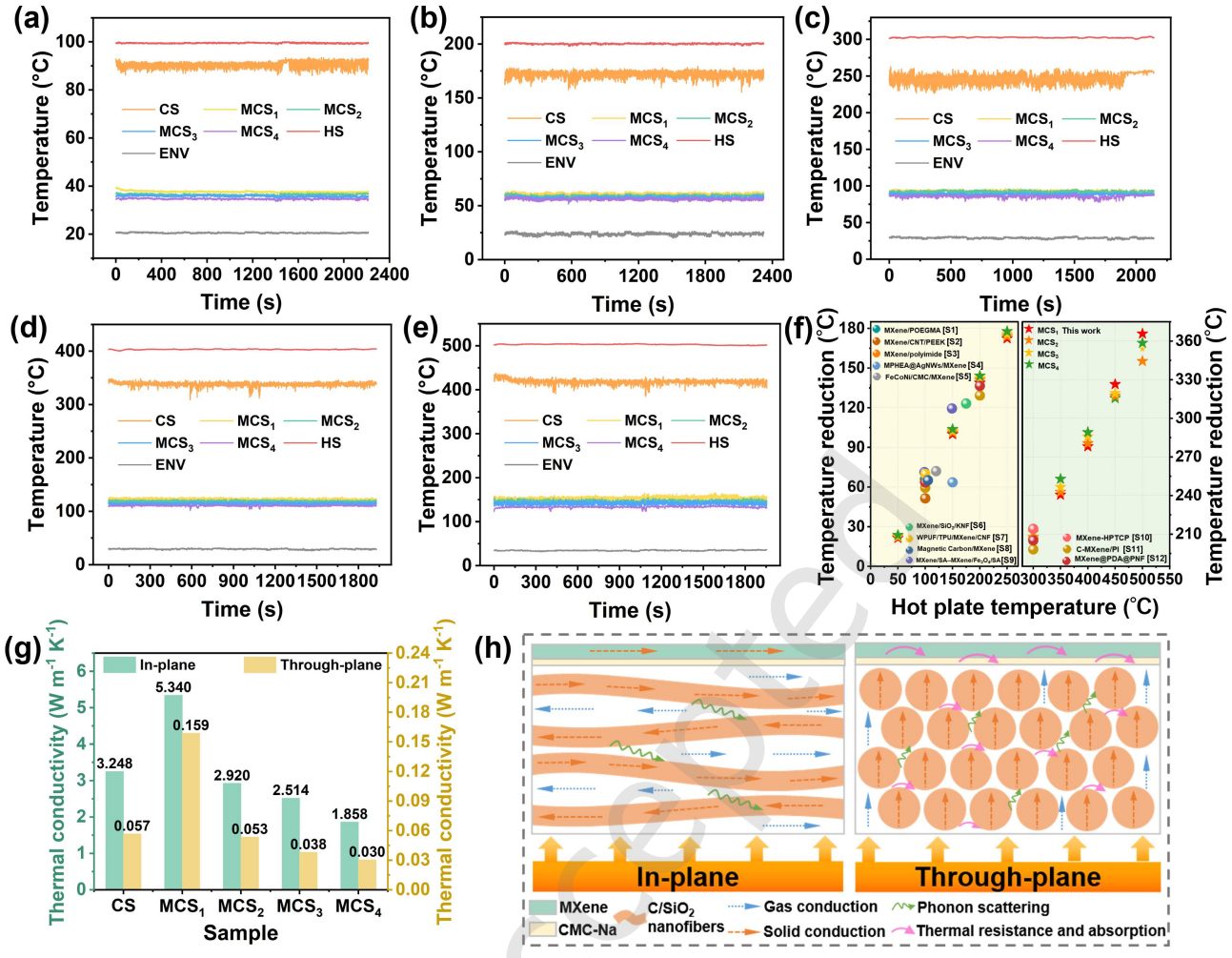


Figure 4 (a–e) Apparent surface temperatures recorded during continuous heating for evaluating thermal stability. (f) Comparison with reported MXene-based infrared stealth materials (in the ESM). (g) In-plane and through-plane thermal conductivities. (h) Schematic illustration of the anisotropic heat transport mechanism.

efficient conversion of electrical energy into heat. Meanwhile, the current–voltage (I–V) curves (Fig. 5(f)) exhibit excellent linearity, indicating Ohmic behavior. Furthermore, the steady-state temperature rise (ΔT) shows an excellent linear correlation with the square of the applied voltage (U^2) (R^2 = 0.999, Fig. 5(g)), which is in good agreement with Joule's law and confirms that the heating behavior originates from resistive Joule heating [42]. Compared with recently reported MXene-based electrothermal materials (Fig. 5(h) and Table S5 in the ESM), MCS_x achieves higher operating temperatures under lower voltages, highlighting its superior low-power electrothermal performance.

Owing to its rapid thermal response, high electrothermal conversion efficiency, and precise temperature regulation capability, the MCS_x composite film holds significant promise for flexible thermal management applications. For smart wearable devices and personal thermal protection, operating voltages of only 1.5–2.0 V provide a comfortable temperature range of approximately 40–60 °C, meeting the requirements for localized thermotherapy and thermal insulation. Furthermore, as illustrated in Fig. 5(i), the surface temperature and infrared radiation intensity can be dynamically regulated by applying voltages of 1.0 or 1.5 V, allowing the infrared emission of the film to closely match that of the surrounding environment. This effectively reduces the infrared contrast between the target and the background, thereby enabling dynamic infrared stealth.

3.4 Flame retardancy and thermal stability

Thermal stability is a key indicator for evaluating the high-temperature service capability of materials. To compare the thermal stability of different components, thermogravimetric analysis (TGA) was performed on the MXene, CS, and MCS_x films. As shown in Figs. S6(a) and S6(b) in the ESM, MXene retained approximately 90% of its initial mass at 800 °C, demonstrating good thermal stability under an inert atmosphere. The CS film exhibited only a slight mass loss of approximately 4.8 wt% and retained 95.2% of its initial mass at 800 °C, indicating excellent high-temperature stability of the C/SiO_2 nanofibrous framework. The TGA curves of MCS_x films are shown in Fig. 6(a), exhibiting two main stages of mass loss: approximately 4.14 wt% below200 °C due to the removal of adsorbed and interlayer water, followed by approximately 4.99 wt% arising from the decomposition of CMC-Na and residual organic components. The MCS_x films retain 89.44 wt% at 800 °C. Their slightly greater mass loss than that of CS is attributed to the removal of MXene surface terminations, decomposition of CMC-Na, and release of interlayer species [43, 44]. Nevertheless, the total mass loss remains below 11 wt%, confirming the high thermal stability of the SiO_2 framework, carbonized fiber network, and MXene components.

Just Accepted

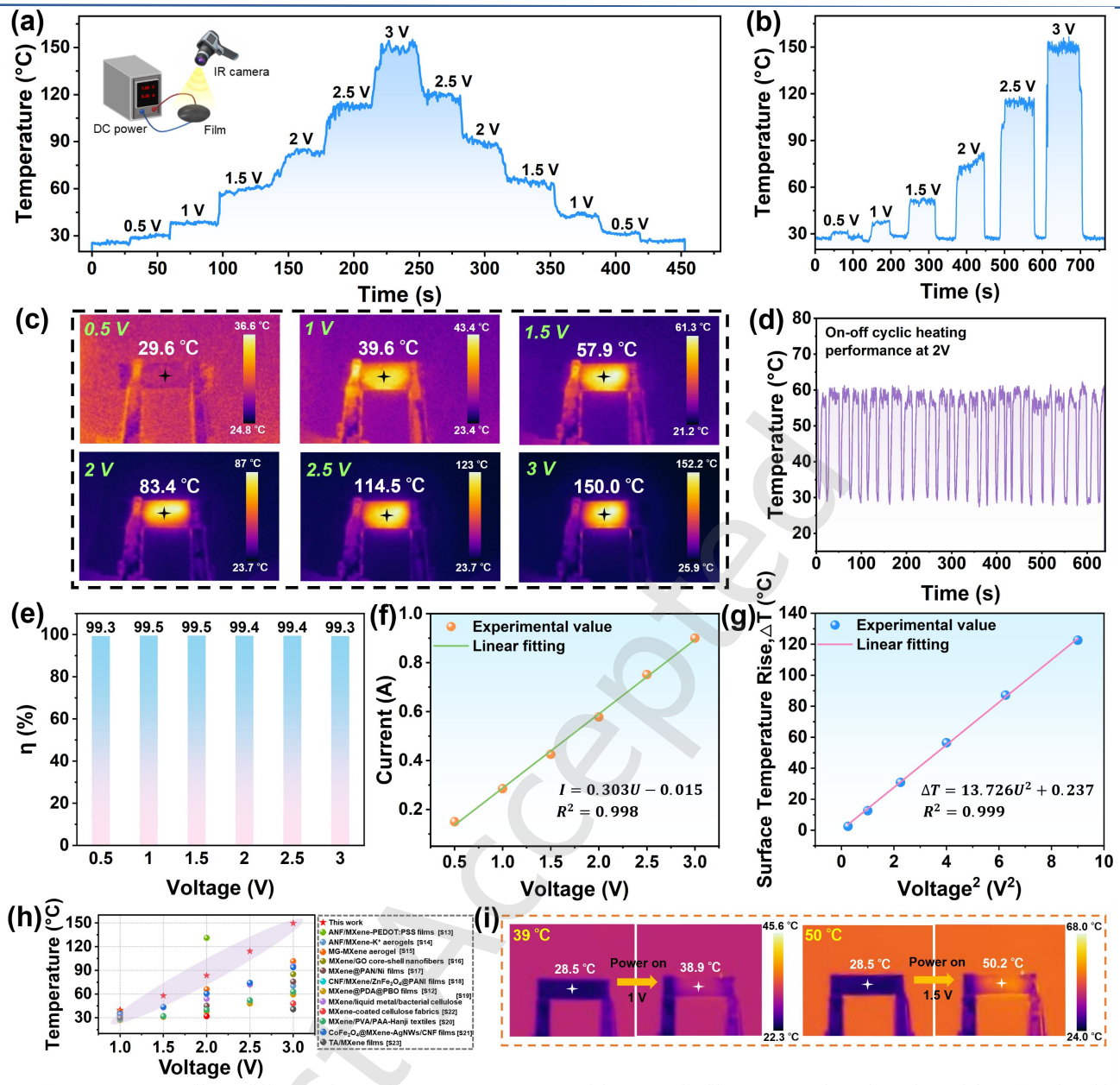


Figure 5 (a) Temperature profiles at different voltages. (b) Temperature response of the composite film upon stepwise voltage rise and drop. (c) Infrared images under different voltages. (d) Cycling stability at 2.0 V. (e) Electrothermal conversion efficiency, (f) current–voltage (I–V) curves with linear fitting, and (g) linear relationship between the steady-state temperature rise (ΔT) and the square of the applied voltage (U^2) under different driving voltages. (h) Comparison with reported MXene electrothermal materials (in the ESM). (i) Demonstration of dynamic infrared stealth.

Microscale combustion calorimetry (MCC) was conducted to evaluate the intrinsic combustion behavior. As shown in Fig. 6(b), the MCS_x film exhibits an ultralow heat release capacity (HRC) of 3.7 J g^{-1} K^{-1}, peak heat release rate (PHRR) of 3.8 W g^{-1}, and total heat release (THR) of 0.3 kJ g^{-1}. The maximum heat release occurs at approximately 288.3 °C and is associated with the degradation of trace organic constituents. These low values indicate negligible generation of combustible volatiles and a low intrinsic fire hazard. The flame tests agree with the MCC results. The CS film maintains its structural integrity after direct flame exposure (Fig. 6(c) and Fig. S7(a) in the ESM), while the MCS_x film remains nonflammable during 30 min of continuous flame exposure without obvious spallation or delamination (Fig. 6(d) and Video S1). The CS film shows no sustained combustion at oxygen concentrations of 25–100 vol%, and the MCS_x film achieves an LOI of 86.4% (Figs. S7(b) and S7(c) in the ESM), confirming its strong resistance to sustained combustion. Considering that the outer MXene layer is directly exposed to an oxidative environment during flame treatment, the oxidation behavior of pristine MXene was further evaluated by TG/DTG analysis in air (Fig. S6(c)). A pronounced mass gain was observed at approximately 350–600 °C, consistent with the oxidation of $Ti_3C_2T_x$ and the formation of TiO_2.

To further evaluate the oxidation behavior of the MCS_x films during flame exposure, MCS_1, containing only one MXene@C/SiO_2 structural unit, was selected as a representative sample for XRD analysis before and after flame treatment. As shown in Fig. 6(e), MCS_1 still retains the characteristic MXene (002) reflection after 30 min of flame exposure, together with only weak TiO_2 diffraction peaks, indicating that MXene oxidation is effectively mitigated even in the simplest MCS_x architecture. In contrast, a pristine MXene film with identical dimensions subjected to the same flame treatment is almost completely converted into TiO_2. These results demonstrate that

Just Accepted

the layered composite structure can effectively retard the oxidative degradation of MXene under the present flame-exposure conditions.

The thermal protection performance was further evaluated using PU foam (Fig. 6(f), Videos S2 and S3). Unprotected PU foam melts severely within approximately 5 s of flame exposure, whereas the MCS_4 film effectively suppresses melting. As illustrated in Fig. 6(g), the MXene surface forms a dense inorganic barrier that restricts oxygen diffusion and volatile release, while the C/SiO_2 layer provides a stable skeleton with low through-plane heat transfer. Char formed from CMC-Na decomposition further reinforces the barrier, and the heterogeneous interfaces increase interfacial thermal resistance. These effects collectively provide thermal stability, flame retardancy, and thermal insulation, demonstrating the potential of MCS_x films for fire protection under high-temperature conditions.

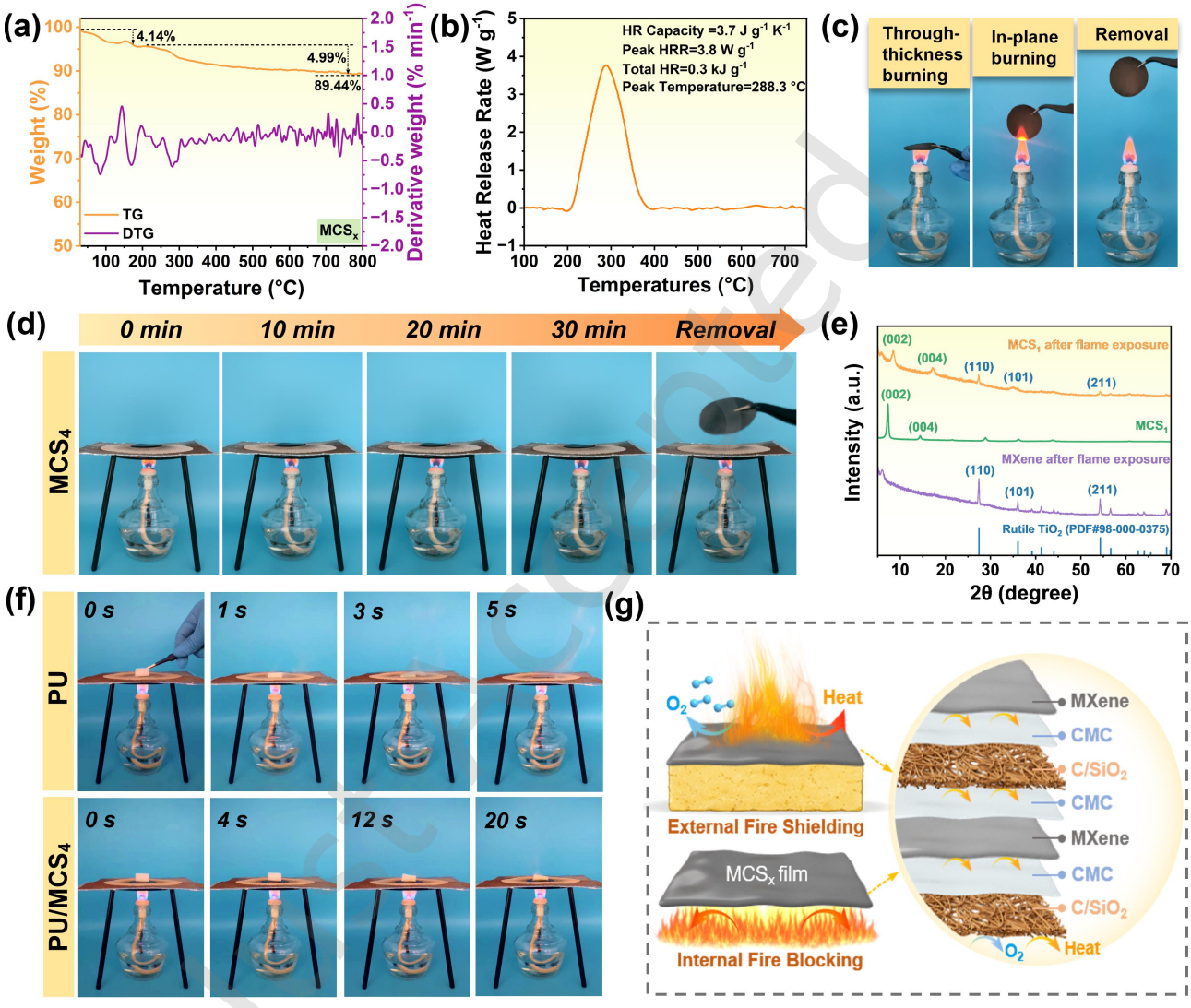


Figure 6 (a) TG/DTG curves of MCS_x films. (b) PHRR, THR, and HRC measured by microscale combustion calorimetry. Flame tests of (c) CS and (d) MCS_4. (e) XRD patterns of pristine MCS_1, MCS_1 after 30 min of flame exposure, and a pristine MXene film subjected to the same flame treatment, together with the standard diffraction pattern of rutile TiO_2. (f) Comparison of the thermal protection performance between pristine PU foam and PU foam protected by an MCS_4 heat-insulating film under continuous flame impingement. (g) Schematic illustration of the flame-retardant and thermal-insulation mechanism.

3.5 Electromagnetic interference shielding performance

Modern communication devices, aerospace systems, and electronic equipment operating in complex electromagnetic environments require not only infrared stealth and thermal protection but also high-performance electromagnetic interference (EMI) shielding to ensure reliable operation [45]. As shown in Figs. 7(a)–7(d), the MCS_x composite films exhibit outstanding EMI shielding performance throughout the X-band, with the relevant parameters calculated according to Eqs. (3)-(8) in the ESM. As the number of structural units increases from 1 to 4, the total shielding effectiveness (SE_T) increases from 50.9 to 71.6 dB. Increasing the number of units raises the film thickness from 88 μm to 260 μm, extending the propagation path of electromagnetic waves, while the abundant MXene@C/SiO_2 interfaces and CMC-Na interlayers promote interfacial polarization, multiple reflections, and scattering within the material. Accordingly, the absorption shielding effectiveness SE_A increases from 30.3 to 52.4 dB, demonstrating improved attenuation of electromagnetic waves propagating into the layered structure. In addition, the low-temperature-carbonized C/SiO_2 nanofiber layer retains residual carbon species, which further contribute to conductive loss and dipolar polarization,

thereby enhancing electromagnetic wave attenuation [26, 46].

The reflection (R), absorption (A), and transmission (T) coefficients (Fig. 7(e)) show R values of approximately 0.98, substantially higher than A, indicating reflection-dominated shielding [2, 47]. It should be noted that SE_A characterizes the attenuation of electromagnetic waves after entering the material, whereas the power coefficients R, A, and T more directly reflect the partitioning of the total incident electromagnetic power among reflection, absorption, and transmission [48, 49]. Therefore, the high R values confirm that the overall EMI shielding behavior of the MCS_x films is reflection-dominated. The strong impedance mismatch between the conductive MXene layer and air reflects most incident waves, while transmitted waves are attenuated by Ohmic loss, interfacial polarization, and

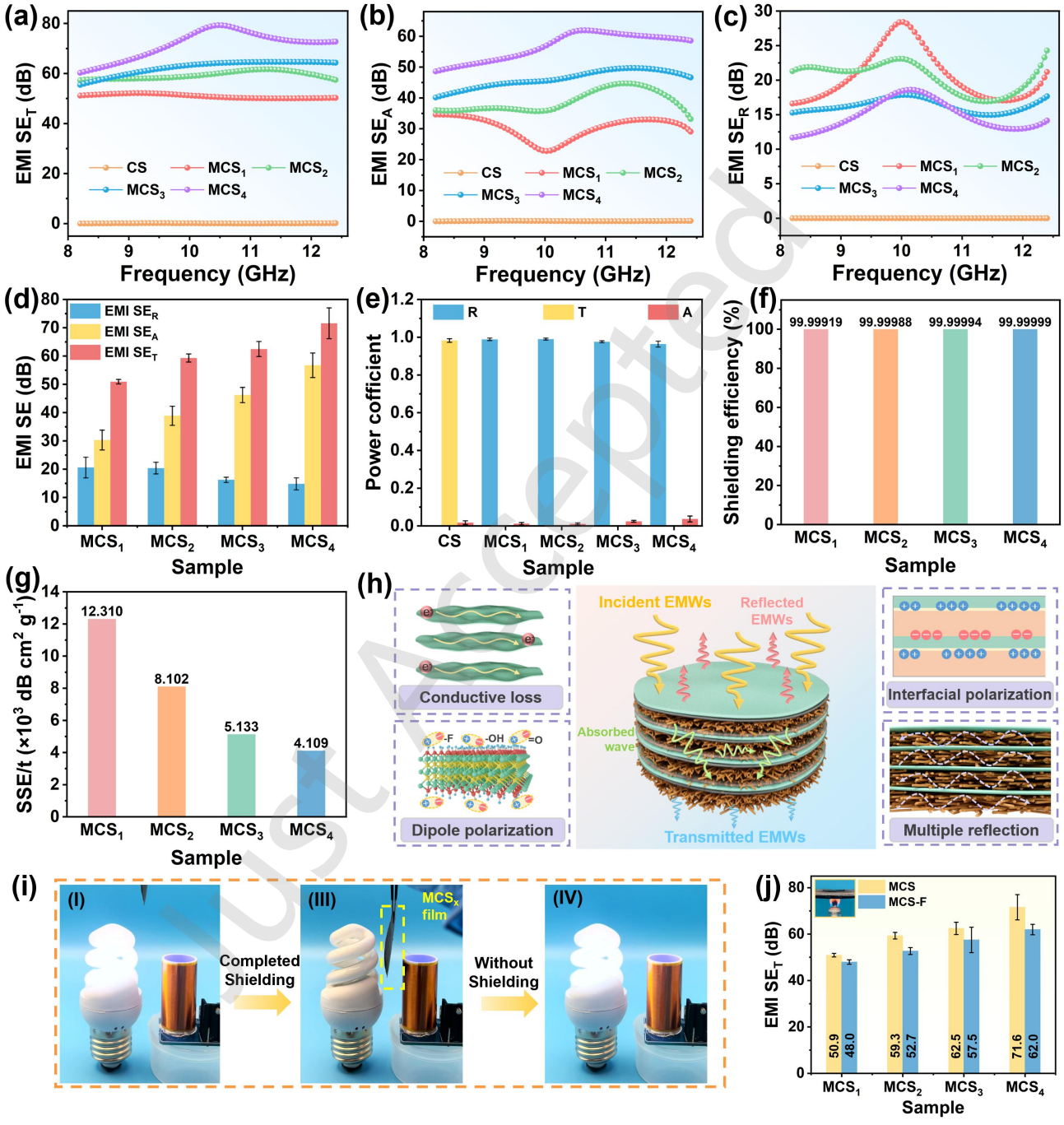


Figure 7 X-band EMI shielding performance: (a) SE_T, (b) SE_A, (c) SE_R, (d) average values of SE_T, SE_A, and SE_R, (e) R, A, and T, (f) shielding efficiency, and (g) thickness-normalized specific shielding effectiveness (SSE/t). (h) Schematic illustration of the EMI shielding mechanism. (i) Tesla-coil demonstration test. (j) EMI shielding performance before and after 30 min of flame exposure.

multiple scattering. Consequently, all samples block more than 99.999% of the incident electromagnetic radiation (Fig. 7(f), Eq. (9) in the ESM). To evaluate the intrinsic shielding capability, the specific shielding effectiveness per unit thickness (SSE/t, Eq. (10) in the ESM) is introduced as the evaluation index. As shown in Fig. 7(g), MCS_1 achieves an exceptionally high SSE/t value of 12310 dB cm^2 g^{-1}. As the number of structural units increases, SSE/t gradually decreases because the improvement in SE_T does not scale proportionally with the increases in film thickness and areal density, leading to a lower mass-normalized

Just Accepted

shielding efficiency. Nevertheless, the multilayer films retain relatively high SSE/t values at higher structural unit numbers.

Fig. 7(h) schematically demonstrates the electromagnetic interference shielding mechanism of the composite film. The highly conductive MXene surface layer reflects most of the incident electromagnetic waves because of the strong impedance mismatch with air. The small fraction of waves entering the layered structure undergoes repeated reflections and scattering at the MXene@C/SiO_2 heterogeneous interfaces and CMC-Na interlayers, thereby extending the propagation path. Simultaneously, differences in dielectric properties and electrical conductivity among the constituent components induce significant interfacial polarization. Moreover, MXene surface groups and defects, together with residual carbon species in the carbonized fiber layer, provide additional conductive and dipolar polarization losses [1, 2]. Collectively, these mechanisms result in highly efficient EMI shielding. A Tesla coil setup was employed to demonstrate the practical shielding capability (Fig. 7(i), Video S4). After inserting an MCS_1 film between the Tesla coil and the bulb, the induced electromagnetic field is effectively blocked, causing the bulb to extinguish immediately. In contrast, the CS film exhibits negligible shielding capability.

Considering potential exposure to fire, the EMI shielding performance was further evaluated before and after 30 min of continuous alcohol flame exposure (MCS_x and MCS_x-F, Fig. 7(j)). The SE_T retention ratios after flame treatment are 94.3%, 88.9%, 92.0%, and 86.6%, respectively, demonstrating substantial retention of the shielding performance. Although partial oxidation of MXene occurs during flame exposure, the distributed MXene layers within the multilayer MXene@C/SiO_2 architecture maintain multiple conductive pathways, thereby reducing the impact of local degradation on the overall shielding performance. These results demonstrate that the multilayer heterostructure contributes to maintaining EMI shielding performance under severe thermal exposure.

4 Conclusions

Layered MXene@C/SiO_2 films were fabricated by electrospinning, pre-oxidation/carbonization, and layer-by-layer assembly. Adjusting the number of structural units tunes film thickness, thermal resistance, and multifunctional performance. The heterogeneous interfaces and CMC-Na interlayers increase interfacial thermal resistance, suppressing through-plane heat transport while preserving preferential in-plane diffusion. MCS_4 consequently achieves a through-plane thermal conductivity of 0.030 W m^{-1} K^{-1} and, with the low emissivity of MXene, an apparent temperature reduction of 365.7 °C on a 500 °C heat source. The continuous MXene conductive network enables controllable Joule heating from 29.5 to 149.6 °C at 0.5–3.0 V, while the conductive layers and heterogeneous interfaces contribute to an EMI shielding effectiveness of up to 71.6 dB. Meanwhile, the thermally stable C/SiO_2-based framework provides effective flame resistance and thermal protection, with high EMI shielding performance retained after 30 min of flame exposure. These results demonstrate that the conductive MXene network, heterogeneous interfaces, and thermally stable nanofibrous framework act synergistically, providing a rational heterostructure design strategy for integrating infrared stealth, EMI shielding, active thermal management, and fire protection.

Electronic Supplementary Material: Supplementary material (including detailed calculation formulas for infrared radiation, electrothermal conversion efficiency, and EMI shielding performance; additional characterization results on MXene structure, carbonized fibrous films, infrared stealth, thermal stability, and flame retardancy; as well as supplementary tables of thermal properties and performance comparisons) is available in the online version of this article.

Data availability

All data needed to support the conclusions in the paper are presented in the manuscript and the Electronic Supplementary Material. Additional data related to this paper may be requested from the corresponding author upon request.

Acknowledgements

This work was supported by the Key Research and Development Program of Shandong Province (Grant Nos. 2021ZLGX01, 2021CXGC010903) and the Natural Science Foundation of Shandong Province (Grant No. ZR2022ME055). The authors acknowledge support from the Open Research Fund of the State Key Laboratory of Coatings for Advanced Equipment and the technical assistance from the Testing and Manufacturing Center for Advanced Materials of Shandong University.

Declaration of competing interest

All the contributing authors report no conflict of interests in this work.

Author contribution statement

N. P.: Conceptualization, Data curation, Formal analysis, Investigation, Writing-original draft. X. Q. Y.: Methodology, Validation. Y. L.: Resources, Supervision. X. C.: Investigation, Validation. M. J. Y.: Conceptualization, Resources, Funding acquisition, Writing-review & editing.

Use of AI statement

None.

References

[1] Wang, Y. J.; Wang, X. C.; Liu, M. Y.; Rong, X.; Fang, S. Y.; Liu, Z. Three-dimensionally crosslinked MXene nanosheet-driven Janus fabrics for dual protection of infrared stealth and electromagnetic shielding. *Adv. Compos. Hybrid Mater.* **2026**, *9*, 273.

[2] Han, Z. Y.; Niu, Y. T.; Shi, X. T.; Pan, D.; Liu, H.; Qiu, H.; Chen, W. H.; Xu, B. B.; El-Bahy, Z. M.; Hou, H.; Elsharkawy, E. R.; Amin, M. A.; Liu, C. T.; Guo, Z. H. MXene@c-MWCNT Adhesive Silica Nanofiber Membranes Enhancing Electromagnetic Interference Shielding and Thermal Insulation Performance in Extreme Environments. *Nano-Micro Lett.* **2024**, *16*, 195.

[3] Hassan, T.; Iqbal, A.; Yoo, B.; Jo, J. Y.; Cakmakci, N.; Naqvi, S. M.; Kim, H.; Jung, S.; Hussain, N.; Zafar, U.; Cho, S. Y.; Jeong, S.; Kim, J.; Oh, J. M.; Park, S.; Jeong, Y.; Koo, C. M. Multifunctional MXene/Carbon Nanotube Janus Film for Electromagnetic Shielding and Infrared Shielding/Detection in Harsh Environments. *Nano-Micro Lett.* **2024**, *16*, 216.

[4] Huo, Q. Q.; Liang, C. B.; Qi, J. M.; He, M. K.; Si, X. F.; Xue, F. P.; Qiu, H.; Gu, J. W. Bioinspired Asymmetric Janus Film Enables Concurrent Dynamic Infrared Camouflage and Electromagnetic Interference Shielding. *Adv. Funct. Mater.* **2026**, *36*, e22330.

[5] Liu, P.; He, Z.; Li, X.; Ding, L.; Liu, S.; Kong, J. Multifunctional Hollow Carbon Microspheres Enable Superior Electromagnetic Wave Response and Corrosion Barrier. *Adv. Mater.* **2025**, *37*, 2500646.

[6] Shen, M. M.; Ni, J. H.; Cao, Y. X.; Yang, Y. Y.; Wang, W. J.; Wang, J. F. Low infrared emitter from $Ti_3C_2T_x$ MXene towards highly-efficient

Just Accepted

electric/solar and passive radiative heating. *J. Mater. Sci. Technol.* **2023**, *133*, 32-40.

[7] Rani, P.; Murthy, V. R. K.; Khadheer Pasha, S. K. Development of MXene based organic polymer nanocomposites as highly efficient Electromagnetic Interference Shielding materials: A review. *Coord. Chem. Rev.* **2026**, *548*, 217104.

[8] Zhao, J.; Liu, H.; Wang, X. D. Decoupling and Dynamic Regulation of Thermal Radiation and Emissivity via an Active/Passive, Environment-Adaptive Metamaterial for Intelligent Infrared Camouflage. *Adv. Funct. Mater.* **2026**, *36*, e30991.

[9] Jing, J. W.; Liu, H.; Wang, X. D. Long-Term Infrared Stealth by Sandwich-Like Phase-Change Composites at Elevated Temperatures via Synergistic Emissivity and Thermal Regulation. *Adv. Funct. Mater.* **2024**, *34*, 2309269.

[10] Wang, Y. Y.; Pang, N.; Liu, S. Y.; Yin, X. Q.; Yu, M. J.; Wang, C. G.; Zhou, C. J. Flexible and high-strength MXene/polyimide nanofiber aerogel membranes achieving infrared stealth through combined thermal control and low emissivity. *Chem. Eng. J.* **2024**, *498*, 155332.

[11] Song, W.; Lan, C.; Du, Z.; Wang, C.; Liu, P. Multi-magnetic regulation of hollow CoNi microspheres via morphological evolution for ultrahigh electromagnetic wave absorption. *Nano Res.* **2026**, *19*, 94909011.

[12] Ding, L.; He, Z.; Zhang, R.; Liu, S.; Geng, W.; Liu, P. Hollow $Zn_{1-x}Co_{2-y}Ni_xFe_yO_4$ spinel via multi-metal ion doping: ultralight and broadband microwave absorber. *Soft Science* **2026**, *6*, 2.

[13] Li, X. L.; Li, M. H.; Li, X.; Fan, X. M.; Zhi, C. Y. Low Infrared Emissivity and Strong Stealth of Ti-Based MXenes. *Research* **2022**, *2022*, 9892628.

[14] Li, Y.; Xiong, C.; Huang, H.; Peng, X. D.; Mei, D. Q.; Li, M.; Liu, G. Z.; Wu, M. C.; Zhao, T. S.; Huang, B. L. 2D $Ti_3C_2T_x$ MXenes: Visible Black but Infrared White Materials. *Adv. Mater.* **2021**, *33*, 2103054.

[15] Wang, L.; Ma, Z. L.; Zhang, Y. L.; Qiu, H.; Ruan, K. P.; Gu, J. W. Mechanically strong and folding-endurance $Ti_3C_2T_x$ MXene/PBO nanofiber films for efficient electromagnetic interference shielding and thermal management. *Carbon Energy* **2022**, *4*, 200-210.

[16] Liu, Y. Y.; Zhang, L. L.; Zhang, R. N.; Shao, S. Q.; Sun, L. N.; Wan, X. Y.; Wang, T. T. Thermal insulating and fire-retardant Si_3N_4 nanowire membranes resistant to high temperatures up to 1300 °C. *J. Mater. Sci. Technol.* **2023**, *155*, 82-88.

[17] Zhu, Z. G.; Li, Z. Y.; Zhong, L. L.; Zhang, R. J.; Cui, F. Y.; Wang, W. Dual-biomimetic superwetting silica nanofibrous membrane for oily water purification. *J. Membr. Sci.* **2019**, *572*, 73-81.

[18] Tao, D. Z.; Li, X.; Dong, Y. B.; Zhu, Y. F.; Yuan, Y. M.; Ni, Q. Q.; Fu, Y. Q.; Fu, S. Y. Super-low thermal conductivity fibrous nanocomposite membrane of hollow silica/polyacrylonitrile. *Compos. Sci. Technol.* **2020**, *188*, 107992.

[19] Mao, X.; Hong, J.; Wu, Y. X.; Zhang, Q.; Liu, J.; Zhao, L.; Li, H. H.; Wang, Y. Y.; Zhang, K. An Efficient Strategy for Reinforcing Flexible Ceramic Membranes. *Nano Lett.* **2021**, *21*, 9419-9425.

[20] Li, S. J.; Meng, X. Y.; Zhu, C. T.; Xu, W. L.; Sun, Y. M.; Lu, X. F.; Dai, Y. Q. Revolutionizing Inorganic Nanofibers: Bridging Functional Elements to a Future System. *ACS Nano* **2025**, *19*, 14579-14604.

[21] Guo, B. F.; Wang, Y. J.; Cao, C. F.; Qu, Z. H.; Song, J.; Li, S. N.; Gao, J. F.; Song, P. A.; Zhang, G. D.; Shi, Y. Q.; Tang, L. C. Large-Scale, Mechanically Robust, Solvent-Resistant, and Antioxidant MXene-Based Composites for Reliable Long-Term Infrared Stealth. *Adv. Sci.* **2024**, *11*, 2309392.

[22] Feng, W. D.; Zou, L. H.; Lan, C. T.; E, S.; Pu, X. Core-Sheath CNT@MXene Fibers Toward Absorption-Dominated Electromagnetic Interference Shielding Fabrics. *Adv. Fiber Mater.* **2024**, *6*, 1657-1668.

[23] Wang, C.; Tsai, C.; Hashimoto, T. Poly(vinyl alcohol) Fibrils with Highly Oriented Amorphous Chains Developed in Electrospun Nanofibers. *Macromolecules* **2024**, *57*, 2191-2204.

[24] Song, Y. L.; Zhao, F.; Li, Z. Z.; Cheng, Z. G.; Huang, H. J.; Yang, M. F. Electrospinning preparation and anti-infrared radiation performance of silica/titanium dioxide composite nanofiber membrane. *RSC Adv.* **2021**, *11*, 23901-23907.

[25] Li, Z. L.; Deng, L. B.; Kinloch, I. A.; Young, R. J. Raman spectroscopy of carbon materials and their composites: Graphene, nanotubes and fibres. *Prog. Mater. Sci.* **2023**, *135*, 101089.

[26] Meng, X. W.; Yu, M.; Wang, C. G. The Design of Ternary Nanofibers with Core–Shell Structure for Electromagnetic Stealthy Antenna. *Adv. Fiber Mater.* **2025**, *7*, 469-480.

[27] Li, Z. F.; Bommier, C.; Chong, Z. S.; Jian, Z. L.; Surta, T. W.; Wang, X. F.; Xing, Z. Y.; Neuefeind, J. C.; Stickle, W. F.; Dolgos, M.; Greaney, P. A.; Ji, X. L. Mechanism of Na-Ion Storage in Hard Carbon Anodes Revealed by Heteroatom Doping. *Adv. Energy Mater.* **2017**, *7*, 1602894.

[28] Ding, J.; Wang, H. L.; Li, Z.; Kohandehghan, A.; Cui, K.; Xu, Z. W.; Zahiri, B.; Tan, X. H.; Lotfabad, E. M.; Olsen, B. C.; Mitlin, D. Carbon Nanosheet Frameworks Derived from Peat Moss as High Performance Sodium Ion Battery Anodes. *ACS Nano* **2013**, *7*, 11004-11015.

[29] Ning, M.; Qiu, G. J.; Wang, X. Y.; Li, B. B.; Li, Z. H.; Zhang, H. Y. Ultrathin carbon nanosheets with carbon composite structure of amorphous carbon and pseudo-graphite domains for high-capacity, stable and fast potassium storage. *J. Power Sources* **2024**, *604*, 234421.

[30] Chen, W. X. N.; Sheng, J.; Chen, D. M.; Sun, B. Q.; Ding, H.; Zhang, L. S.; Liu, B.; Ren, Q. T.; Zhang, D. Y.; Fang, Y. H.; Lu, X. C.; Wu, Y. Y.; Lan, Y.; Zou, Y. C.; Zhang, P.; Yang, X. M.; Zhang, P. C.; Wang, Z. Q.; Lin, Q. R.; Tan, M. Y.; Zhang, W. Z.; Cheng, Y.; Li, W. L.; Wang, L. D.; Dong, S.; Du, S. Y.; Han, J. C.; Fei, W. D.; Zhang, X. H. Graphene–amorphous carbon with interwoven networks for enhanced strength. *Nat. Commun.* **2025**, *16*, 10513.

[31] Anggoro, D.; Sudarsono; Purwandari, E.; Baqiya, M. A.; Ramli, M. M.; Nakajima, H.; Yudoyono, G.; Darminto Tailoring conductive polyvinyl alcohol nanofibers: thermal-induced structural evolution in nitrogen for energy storage device. *Discover Materials* **2025**, *5*, 16.

[32] Ran, X.; Liu, C. J.; Chen, B. Surface tension-mediated assembly of MXene films for high-performance electromagnetic interference shielding and thermal management applications. *Carbon* **2026**, *247*, 121028.

[33] Zhou, T. Z.; Yu, Y. Z.; He, B.; Wang, Z.; Xiong, T.; Wang, Z. X.; Liu, Y. T.; Xin, J. W.; Qi, M.; Zhang, H. Z.; Zhou, X. H.; Gao, L. H.; Cheng, Q. F.; Wei, L. Ultra-compact MXene fibers by continuous and controllable synergy of interfacial interactions and thermal drawing-induced stresses. *Nat. Commun.* **2022**, *13*, 4564.

[34] Li, X. H.; Ran, F. T.; Yang, F.; Long, J.; Shao, L. Advances in MXene Films: Synthesis, Assembly, and Applications. *Trans. Tianjin Univ.* **2021**, *27*, 217-247.

[35] Moreno, Y. P.; Cardoso, M. B.; Ferrão, M. F.; Moncada, E. A.; Dos Santos, J. H. Z. Effect of $SiCl_4$ on the preparation of functionalized mixed-structure silica from monodisperse sol–gel silica nanoparticles. *Chem. Eng. J.* **2016**, *292*, 233-245.

[36] Wang, H. T.; Wu, Y. S.; Guo, S.; Dong, C. L.; Ding, M. Y. γ-Valerolactone converting to butene via ring-opening and decarboxylation steps over amorphous SiO_2-Al_2O_3 catalyst. *Mol. Catal.* **2020**, *497*, 111218.

[37] Duong, T. T.; Kim, S. H.; Kim, J. Amphiphilic silane-MXene hybrids for high-performance flexible symmetric supercapacitors via additive-free processing. *J. Mater. Chem. A* **2026**, *14*, 4801-4812.

[38] Parker, T.; Zhang, D. Z.; Bugallo, D.; Shevchuk, K.; Downes, M.; Valurouthu, G.; Inman, A.; Chacon, B.; Zhang, T.; Shuck, C. E.; Hu, Y.; Gogotsi, Y. Fourier-Transform Infrared Spectral Library of MXenes. *Chem. Mat.* **2024**, *36*, 8437-8446.

[39] Näslund, L.; Persson, P. O. Å.; Rosen, J. X-ray Photoelectron Spectroscopy of Ti_3AlC_2, $Ti_3C_2T_z$, and TiC Provides Evidence for the Electrostatic Interaction between Laminated Layers in MAX-Phase Materials. *J. Phys. Chem. C* **2020**, *124*, 27732-27742.

[40] A., K.; P., C.; T., H. Selective Fabrication of SiC/Si Diodes by Excimer Laser Under Ambient Conditions. *IEEE Electron Device Lett.* **2016**, *37*, 142-145.

[41] Khadka, J.; Ganorkar, S.; Lee, D. Investigation of thermal emissivity and electrical resistivity of highly reflective nano-grained metal films. *Appl. Therm. Eng.* **2025**, *268*, 125854.

[42] Yu, S. K.; Bao, Y.; Zhang, W. B.; Gao, L.; Guo, R. Y.; Liu, C.; Ma, J. Z. Long-term infrared stealth at Joule heating of AgNWs/bacterial cellulose/carbon fibers fabric by mimicking beetle elytra multi-layered composite structure via synergistic effect of emissivity and thermal regulation. *Adv. Compos. Hybrid Mater.* **2025**, *8*, 419.

[43] Wu, J. Y.; Xu, S. K.; Li, Y. B.; Mo, T. M.; Wang, Y. H.; Yang, Y. Competitive oxidation mechanism endows MXene-based supercapacitors with high-temperature tolerance and self-healing capability. *Energy Storage Mater.* **2025**, *74*, 103928.

[44] De Cachinho Cordeiro, I. M.; Chen, T. B. Y.; Yuen, A. C. Y.; Lin, B.; Jia, M.; Wang, W.; Chen, Q.; Yang, W. J.; Tian, C.; Wang, C.; Yeoh, G. H. Molecular dynamics insights into Ti_3C_2 MXene/chitosan composite

Not Accepted

as a flame-retardant barrier. *Commun. Mater.* **2025**, *6*, 268.

[45] Fu, J. S.; Lian, W. W.; Deng, Y. K.; Fang, Z. X.; Cheng, Q. F. Isotropic thermal insulating cuttlebone-inspired MXene aerogel. *Natl. Sci. Rev.* **2025**, *12*, nwaf342.

[46] Wu, Q.; Ma, Z.; Wang, C.; Tao, Y.; Wang, S.; Jin, Z.; Gao, T.; Li, C.; Liu, P. Carbon nanofibers with small-sized Co nanoparticles and structural defects via a confined-coordination growth strategy toward electromagnetic wave absorption. *J. Adv. Ceram.* **2025**, *14*, 9221210.

[47] Li, Y. K.; Liu, M. X.; Li, C. Y.; Cui, K. P.; Li, L. B.; Jia, L. C. Aramid nanofibers-assisted graphite films for efficient electromagnetic interference shielding. *Compos. Pt. B-Eng.* **2025**, *296*, 112269.

[48] Wan, Y.; Zhu, P.; Yu, S.; Sun, R.; Wong, C.; Liao, W. Anticorrosive, Ultralight, and Flexible Carbon-Wrapped Metallic Nanowire Hybrid Sponges for Highly Efficient Electromagnetic Interference Shielding. *Small* **2018**, *14*, 1800534.

[49] Nguyen, N. K.; Kim, D.; Phan, V. Q.; Kim, M.; Park, P.; Nah, J. Perspectives on absorption-dominant electromagnetic interference shielding materials with MXene and carbon-based polymer composites. *Carbon* **2025**, *238*, 120276.

Just Accepted

Electronic Supplementary Material

MXene@C/SiO_2 composite films with layered heterostructures for high-temperature infrared stealth, electromagnetic interference shielding, and fire safety

Nan Pang[1,2], Xiaoqing Yin[1,2], Yi Lu[3], Xiao Cheng[1] ✉, Meijie Yu[1,2] ✉

[1] *State Key Laboratory of Coatings for Advanced Equipment, School of Materials Science & Engineering, Shandong University, Jinan 250061, China*
[2] *Shandong Key Laboratory of Carbon Fiber and Composite Materials Manufacture and Application, Weihai 264211, China*
[3] *Shandong Institute of Nonmetallic Materials, Jinan 250031, China*

✉ Address correspondence to Meijie Yu, yumeijie@sdu.edu.cn; Xiao Cheng, chengxiao@sdu.edu.cn

Supporting information to https://doi.org/10.26599/NR.2026.94909295

INFORMATION ABOUT ELECTRONIC SUPPLEMENTARY MATERIAL. TEM image, FTIR spectrum, and XRD patterns of MXene; SEM images and fiber diameter distributions of fibrous membranes carbonized at different temperatures; areal shrinkage ratios of carbonized fibrous membranes; infrared thermographic images of MCS_x composite films under different heat-source temperatures; apparent surface temperature evolution and thermal stability of MCS_x composite films; TG/DTG curves of MXene and CS films under N_2 and MXene in air; morphological changes of the MCS_1 composite film after flame exposure and limiting oxygen index (LOI) tests; surface radiation temperatures and temperature differences under different heat-source temperatures; comparison of infrared stealth performance with previously reported MXene-based materials; measured in-plane and through-plane thermal properties; comparison of Joule heating performance with recently reported MXene-based materials; calculation equations for infrared signal intensity, electrothermal conversion efficiency, electromagnetic interference shielding parameters, shielding efficiency, and thickness-normalized specific shielding effectiveness.

Just Accepted

1. Supplementary Figures S1-S7

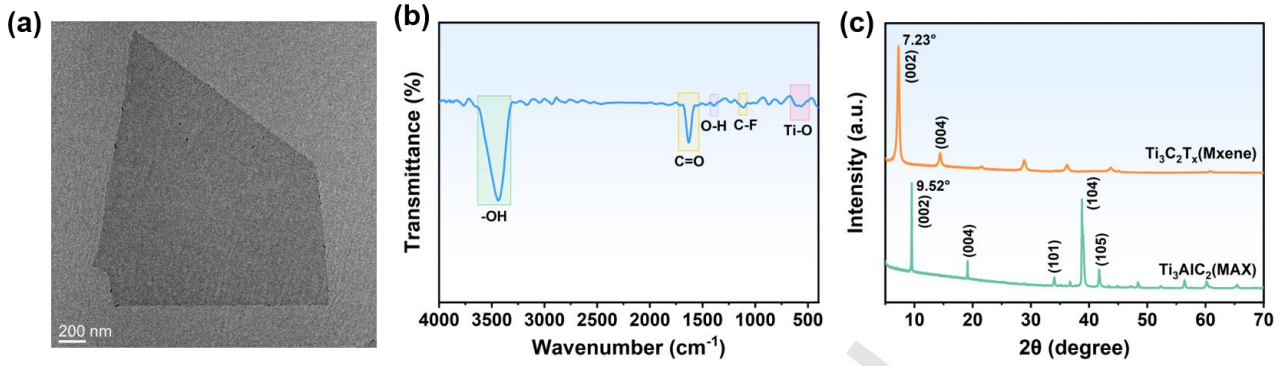


Figure S1 (a) TEM image of MXene nanosheets showing their typical two-dimensional morphology. (b) FTIR spectrum of MXene. (c) XRD patterns of Ti_3AlC_2 and $Ti_3C_2T_x$ MXene.

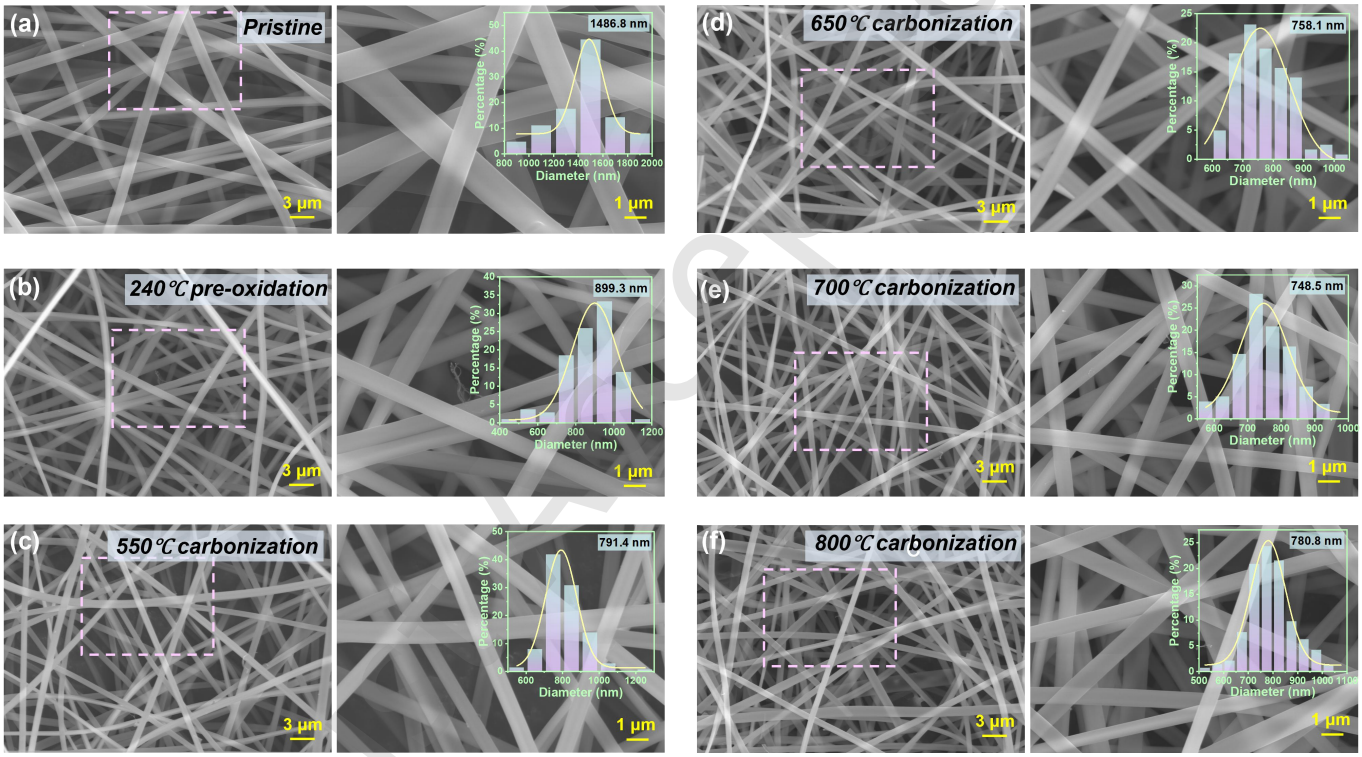


Figure S2 (a-f) SEM images of fibrous membranes carbonized at different temperatures and the corresponding fiber diameter distributions.

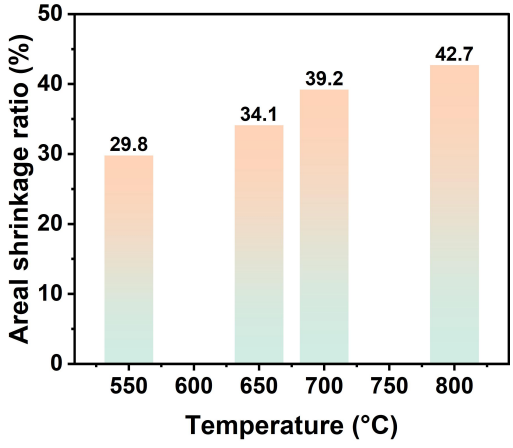


Figure S3 Areal shrinkage ratios of fibrous membranes carbonized at different temperatures.

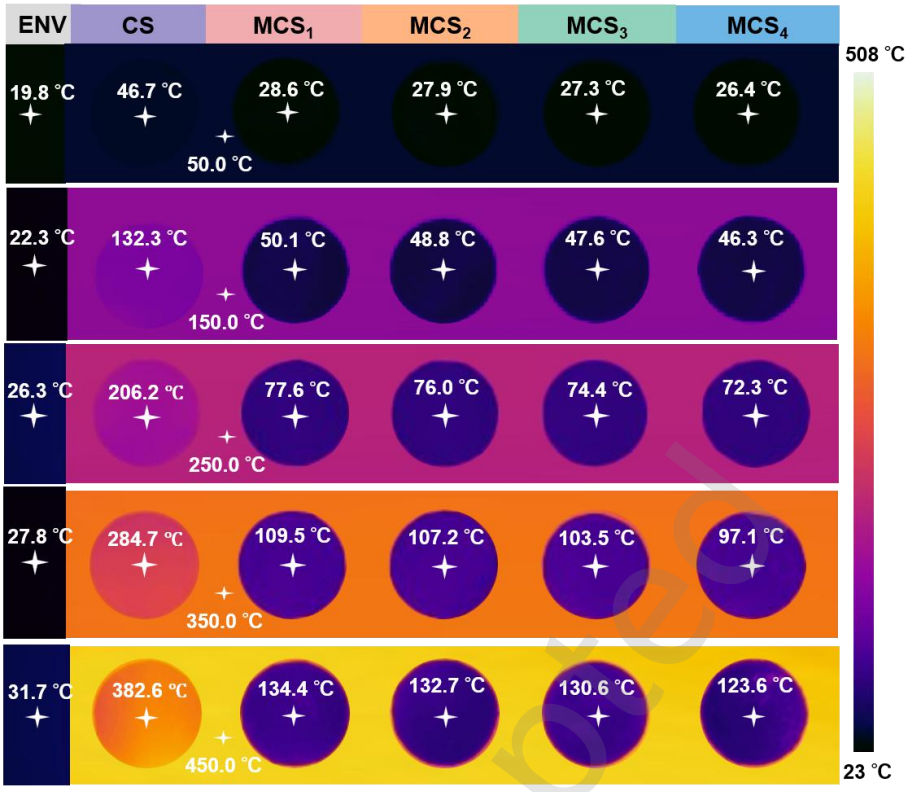


Figure S4 Infrared thermographic images of the composite films under different heat-source temperatures.

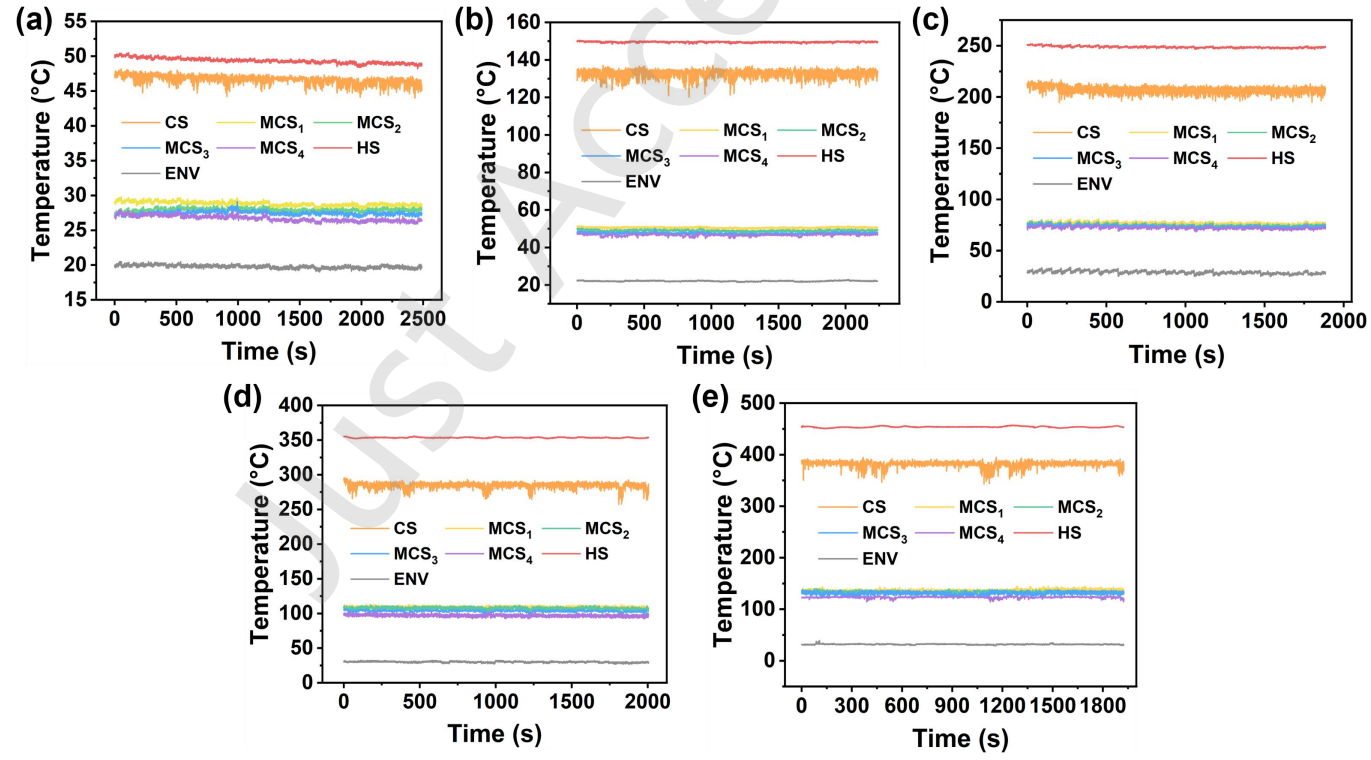


Figure S5 (a-e) Apparent surface temperature evolution of the MCS_x composite films under different heat-source temperatures and their thermal stability.

Just Accepted

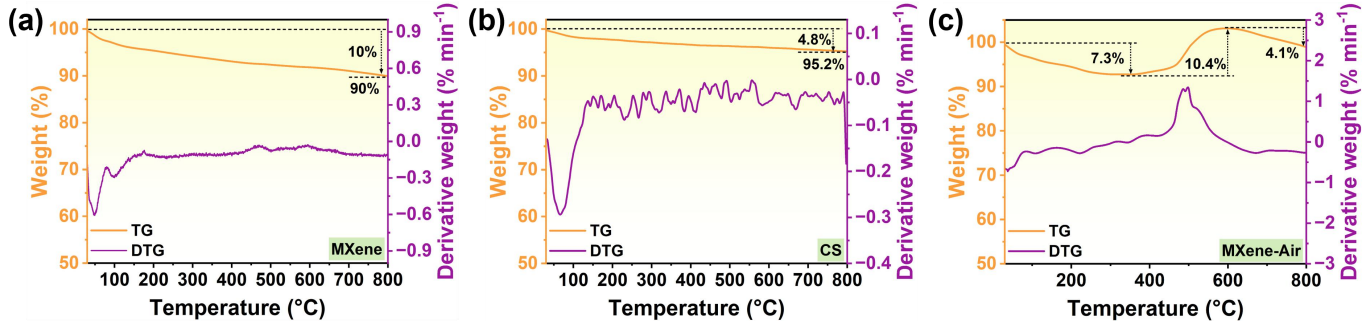


Figure S6 TG/DTG curves of (a) MXene under N_2, (b) CS films under N_2, and (c) MXene in air.

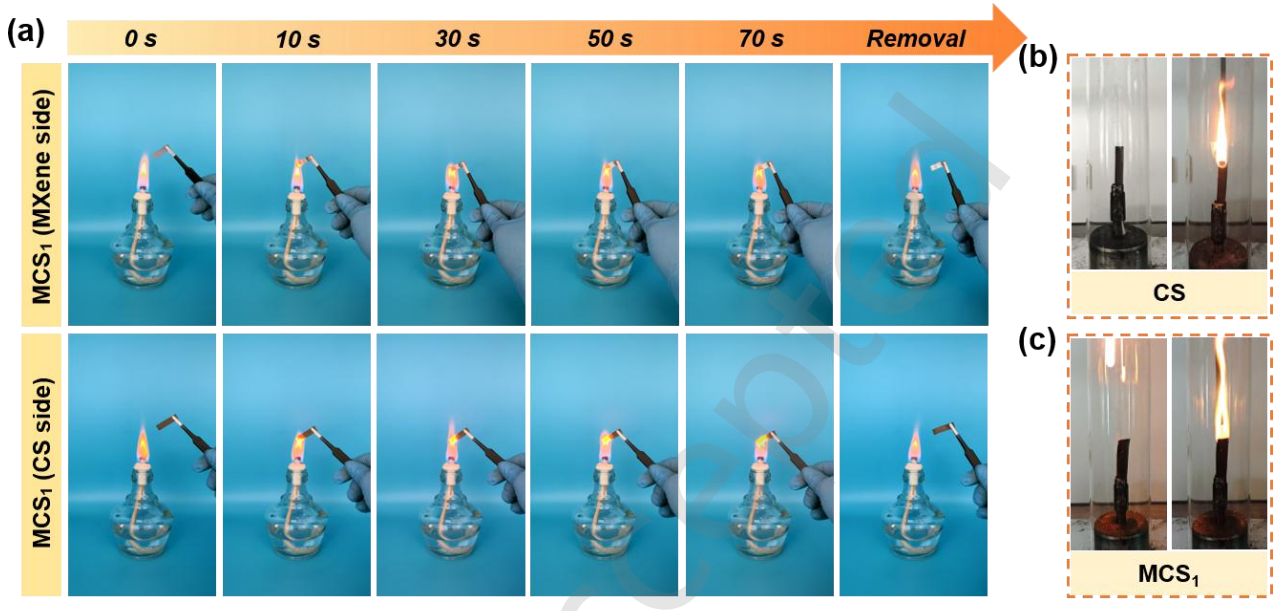


Figure S7 (a) Morphological changes of both sides of the MCS_1 composite film after alcohol-lamp flame exposure. Limiting oxygen index (LOI) tests of (b) the CS film and (c) the MCS_1 composite film.

2. Supplementary Tables S1-S5

Table S1 Surface radiation temperature of MCS_x composite films (T_{film}) and the temperature difference between the heat source and film surface ($T_{hot\ plate}$ -T_{film}) under different heat-source temperatures.

$T_{hot\ plate}$ (℃)	CS (℃)		MCS_1 (℃)		MCS_2 (℃)		MCS_3 (℃)		MCS_4 (℃)	
	T_{film}	$T_{hot\ plate}$ -T_{film}	T_{film}	$T_{hot\ plate}$ -T_{film}	T_{film}	$T_{hot\ plate}$ -T_{film}	T_{film}	$T_{hot\ plate}$ -T_{film}	T_{film}	$T_{hot\ plate}$ -T_{film}
50	46.7	3.3	28.6	21.4	27.9	22.1	27.3	22.7	26.4	23.6
100	90.8	9.2	37.7	62.3	36.3	63.7	35.5	64.5	34.7	65.3
150	132.3	17.7	50.1	99.9	48.8	101.2	47.6	102.4	46.3	103.7
200	171.8	28.2	61.2	138.8	59.2	140.8	57.9	142.1	55.9	144.1
250	206.2	43.8	77.6	172.4	76	174	74.4	175.6	72.3	177.7
300	245.3	54.7	93.8	206.2	92.4	207.6	88.9	211.1	85.4	214.6
350	284.7	65.3	109.5	240.5	107.2	242.8	103.5	246.5	97.1	252.9
400	338.5	61.5	121.9	278.1	119.6	280.4	114.2	285.8	110.9	289.1
450	382.6	67.4	134.4	315.6	132.7	317.3	130.6	319.4	123.6	326.4
500	418.3	81.7	155.6	344.4	146.2	353.8	141.5	358.5	134.3	365.7

Just Accepted

Table S2 Comparison of the infrared stealth performance of this work with previously reported MXene-based infrared stealth materials [S1-S12].

	Object temperature ($T_{hot\ plate}$) (℃)	Radiation temperature (T_{film}) (℃)	Temperature reduction ($T_{hot\ plate}$ -T_{film}) (℃)	Reference
MXene/POEGMA	100	33.8	66.2	[S1]
MXene/CNT/PEEK	100	48.6	51.4	[S2]
MXene/polyimide	300	93.8	206.2	[S3]
MPHEA@AgNWs/MXene	150	86.5	63.5	[S4]
FeCoNi/CMC/MXene	120	48	72	[S5]
MXene/SiO_2/KNF	175	51.9	123.1	[S6]
WPUF/TPU/MXene/CNF	100	30.1	69.9	[S7]
Magnetic Carbon/MXene	105	40	65	[S8]
MXene/SA-MXene/Fe_3O_4/SA	98.5	27.3	71.2	[S9]
	149.1	29.7	119.4	
MXene-HPTCP	300	86	214	[S10]
C-MXene/PI	100	40.6	59.4	[S11]
	200	70.8	129.2	
	300	101.8	198.2	
MXene@PDA@PNF	100	36.6	63.4	[S12]
	200	63.5	136.5	
	300	94.8	205.2	
MCS_1	Table S1	Table S1	Table S1	This work
MCS_2	Table S1	Table S1	Table S1	This work
MCS_3	Table S1	Table S1	Table S1	This work
MCS_4	Table S1	Table S1	Table S1	This work

Table S3 Measured in-plane thermal properties of the films, including thermal conductivity, thermal diffusivity, specific heat capacity, and density.

Sample	Thermal conductivity, λ ($W\ m^{-1}\ K^{-1}$)	Thermal diffusion, α ($mm^2\ s^{-1}$)	Specific heat capacity, C_p ($J\ g^{-1}\ K^{-1}$)	Density, ρ ($g\ cm^{-3}$)
CS	3.248	7.290	1.720	0.259
MCS_1	5.340	9.622	1.480	0.375
MCS_2	2.920	4.919	1.062	0.559
MCS_3	2.514	3.974	0.900	0.703
MCS_4	1.858	2.640	0.959	0.734

Table S4 Measured through-plane thermal properties of the films, including thermal conductivity, thermal diffusivity, specific heat capacity, and density.

Sample	Thermal conductivity, λ ($W\ m^{-1}\ K^{-1}$)	Thermal diffusion, α ($mm^2\ s^{-1}$)	Specific heat capacity, C_p ($J\ g^{-1}\ K^{-1}$)	Density, ρ ($g\ cm^{-3}$)
CS	0.057	0.127	1.720	0.259
MCS_1	0.159	0.286	1.480	0.375
MCS_2	0.053	0.090	1.062	0.559
MCS_3	0.038	0.060	0.900	0.703
MCS_4	0.030	0.043	0.959	0.734

Table S5 Comparison of the Joule heating performance of this work with recently reported MXene-based Joule heating materials [S13-S23].

	Voltage (V)	Temperature (℃)	Reference
ANF/MXene-PEDOT:PSS	2	131.1	[S13]
ANF/MXene-K^+	3	70.3	[S14]
MG-MXene aerogel	1	37.4	[S15]
	2	66	
	3	101.5	
MXene/GO core-shell nanofibers	3	85	[S16]
MXene@PAN/Ni films	1	35.8	[S17]
	2	45.1	
	3	75.6	
CNF/MXene/$ZnFe_2O_4$@PANI	3	41.2	[S18]
MXene@PDA@PBO	1	27	[S12]
	1.5	31	
	2	38	
	2.5	48	
	3	59.4	
MXene/liquid metal/bacterial cellulose	1	32.4	[S19]

Just Accepted

	1.5	43.1	
	2	53.8	
	2.5	72	
	3	95.5	
MXene/PVA/PAA-Hanji (MPP-H)	1	28	[S20]
	1.5	32	
	2	40	
	2.5	52	
	3	63	
$CoFe_2O_4$@MXene-AgNWs/CNF	1	34.6	[S21]
	1.5	43.6	
	2	60.6	
	2.5	74.2	
	3	93.7	
MXene-coated cellulose fabrics	1	28	[S22]
	2	32	
	3	48	
TA/MXene composite film	1	29.9	[S23]
	3	40.6	
MCS_x	1	39.6	This work
	1.5	57.9	
	2	83.4	
	2.5	114.5	
	3	150	

3. Supplementary Equations

To quantitatively evaluate the respective contributions of thermal insulation arising from anisotropic heat transport and low infrared emissivity to infrared stealth performance, the infrared signal intensity (I) was calculated by integrating the emitted thermal radiation over the atmospheric window (8–14 μm) according to Planck's law of thermal radiation [S24, S25].

$$I = 10\log_{10}\left(\frac{\int_{8\mu m}^{14\mu m}\varepsilon(\lambda)M(\lambda,T)\,d\lambda}{\int_{8\mu m}^{14\mu m}M(\lambda,T_{ref})\,d\lambda}\right) \quad (1)$$

where $M(\lambda,T)$ is the spectral radiance of an ideal blackbody at temperature T, $\varepsilon(\lambda)$ is the wavelength-dependent emissivity, and λ denotes the wavelength. T_{ref} represents the reference temperature of the blackbody target. Accordingly, the infrared signal intensity of the reference blackbody is defined as 0 dB.

The electrothermal conversion efficiency (η) at different applied voltages was determined according to Eq. (2) [S26]:

$$\eta = \frac{H_{in}-H_{loss}}{H_{in}}1 - \frac{\bar{\varepsilon}\sigma S(T^4-T_a{}^4)}{UI} \quad (2)$$

where T and T_a represent the temperatures of the film and the surrounding environment (K), respectively. σ is the Stefan–Boltzmann constant (5.67032×10^{-8} W m^{-2} K^{-4}), $\bar{\varepsilon}$ denotes the average infrared emissivity, S is the film area, and U and I correspond to the applied voltage and measured current, respectively.

The electromagnetic interference (EMI) shielding performance in the X-band (8.2–12.4 GHz) was measured using a vector network analyzer (Agilent N5244A PNA-X). Based on the measured scattering (S) parameters, the reflection coefficient (R), absorption coefficient (A), and transmission coefficient (T) were calculated, from which the reflection shielding effectiveness (SE_R), absorption shielding effectiveness (SE_A), and total shielding effectiveness (SE_T) were obtained. SE_M can be ignored when SE_A exceeds 15 dB. The equations are provided below [S27].

$$R = |S_{11}|^2 \quad (3)$$

$$T = |S_{12}|^2 \quad (4)$$

$$A = 1 - R - T \quad (5)$$

$$SE_R = -10\log(1-R) \quad (6)$$

$$SE_A = -10\log\left(\frac{T}{1-R}\right) \quad (7)$$

$$SE_T = 10\log\frac{1}{T} = SE_R + SE_A + SE_M \quad (8)$$

The shielding efficiency (SE), defined as the percentage of incident electromagnetic waves effectively blocked by the material, was calculated using Eq. (9) [S28].

$$SE = \left[1 - \left(\frac{1}{10^{\frac{SE_T}{10}}}\right)\right] \times 100\% \quad (9)$$

To evaluate the intrinsic EMI shielding performance, the thickness-normalized specific shielding effectiveness (SSE/t, dB cm^2 g^{-1}) was further calculated according to Eq. (10), where ρ and t denote the density (g cm^{-3}) and thickness (cm) of the specimen, respectively [S28].

$$\mathrm{SSE/t} = \frac{SE_T}{\rho t} \quad (10)$$

References

[S1] Liu, Z. X.; Zhang, G. X.; Chen, W. T.; Wang, J. X.; Zhang, B. L.; Zhang, Q. Y. Robust biomimetic $Ti_3C_2T_x$ nanocomposite films enhanced by mussel-inspired polymer for highly efficient electromagnetic shielding and thermal camouflage. *Carbon* **2022**, *196*, 410-421.

Just Accepted

[S2] Bai, Y.; Guo, C. Q.; Liang, L. B.; Wang, S. D.; Mei, X. H.; Lu, Y. X.; Jiao, J. P.; Wang, G. B.; Zhang, S. L. High-strength crosslinked MXene/CNT/PEEK composites for electromagnetic interference shielding and infrared camouflage in extreme environments. *Chem. Eng. J.* **2025**, *522*, 167579.

[S3] Wang, Y. Y.; Pang, N.; Liu, S. Y.; Yin, X. Q.; Yu, M. J.; Wang, C. G.; Zhou, C. J. Flexible and high-strength MXene/polyimide nanofiber aerogel membranes achieving infrared stealth through combined thermal control and low emissivity. *Chem. Eng. J.* **2024**, *498*, 155332.

[S4] Bai, Y.; Zhang, B.; Ma, J.; Cheng, Y.; Cui, P.; Kang, Y.; Wu, F.; Chen, C.; Huang, W. Adhesion Strategy for Cross-Linking AgNWs/MXene Janus Membrane: Stretchable and Self-Healing Electromagnetic Shielding and Infrared Stealth Capabilities. *Small* **2025**, *21*, 2408950.

[S5] Li, C.; Liang, L. L.; Zhang, B. S.; Yang, Y.; Ji, G. B. Synergistic customization of interfacial engineering MXene-integrated aerogels enable multifunctional radar-infrared stealth. *Chem. Eng. J.* **2025**, *520*, 166211.

[S6] Zhang, S.; Wu, F. S.; Hu, F. Y.; Hu, P. Y.; Li, M. P.; Zeng, P.; Zhang, P. G.; Wang, T. Y.; Chen, S. S.; Liu, J.; Cai, L. Z.; Sun, Z. M. Cross-dimensional assembly of MXene/SiO2/KNF composite aerogels for radar and infrared stealth. *Mater. Horiz.* **2025**, *12*, 6862-6874.

[S7] Wang, Q. H.; Zhang, J.; Zhou, Z. H.; Zhao, J. Q.; Yi, Y.; Feng, S. Y.; Sui, Z. Y.; Zhang, W.; Lu, C. H. Sandwich-Structured Mxene/Waste Polyurethane Foam Composites For Highly Efficient Electromagnetic Interference, Infrared Shielding and Joule Heating. *Small* **2024**, *20*, 2309803.

[S8] Dong, M. Y.; Zhou, L.; Wang, J. H.; Wang, G.; Zhang, X. N.; Guo, S. J.; Wu, N. N. Versatile cellulose nanofiber assisted preparation of magnetic Carbon/MXene aerogel for broadband microwave absorption and infrared stealth. *Carbon* **2026**, *252*, 121414.

[S9] Li, J. D.; Liang, C. Y.; Lin, C. W.; Wang, Y. N.; Liang, Y. J.; Dong, D. W. Superelastic MXene-based double-layer aerogels for absorption-dominated EMI shielding and infrared stealth. *Carbon* **2026**, *247*, 121066.

[S10] Fang, C. J.; Song, Y. B.; Gu, Y. C.; Liu, P. J.; Chen, W. H. Flame-induced performance enhancement of MXene-based nanocomposite sponge for infrared stealth and strain sensing. *Chem. Eng. J.* **2024**, *502*, 158091.

[S11] Zhang, S.; Liang, C. M.; Zhou, L.; Wu, J. T.; Koo, M. C.; Wu, Z. X.; Chen, Y. T.; Wang, G. S. Heterolayered Carbonized MXene/Polyimide Aerogel for Low-Reflection Electromagnetic Interference Shielding and Multi-Spectrum Compatible Protection. *Nano-Micro Lett.* **2026**, *18*, 204.

[S12] Pang, N.; Cheng, X.; Yin, X. Q.; Wang, Y. Y.; Liu, W.; Yu, M. J.; Wang, C. G.; Zhou, C. J. Janus-structured ion-bridged MXene@PDA@PNF flexible composite films for synergistic infrared stealth, Joule thermal management, and EMI shielding. *J. Mater. Sci. Technol.* **2026**, *259*, 292-306.

[S13] Zhou, B.; Song, J. Z.; Wang, B.; Feng, Y. Z.; Liu, C. T.; Shen, C. Y. Robust double-layered ANF/MXene-PEDOT:PSS Janus films with excellent multi-source driven heating and electromagnetic interference shielding properties. *Nano Res.* **2022**, *15*, 9520-9530.

[S14] Wang, X. L.; Hu, X. P.; Liu, Z. G.; Zhu, C. B.; Shen, R.; Quan, B. Q.; Yan, X. Y.; Wang, W. L.; Lu, X.; Qu, J. P. Interpenetrating double-network ANF/MXene-K^+ aerogels enable integrated electromagnetic interference shielding, infrared camouflage, and Joule Heating in adaptive multifunctional systems. *Nano Res.* **2025**, *18*, 94907702.

[S15] Qi, C. Z.; Min, P.; Zhou, X. F.; Jin, M.; Sun, X.; Wu, J. J.; Liu, Y. J.; Zhang, H. B.; Yu, Z. Z. Multifunctional Asymmetric Bilayer Aerogels for Highly Efficient Electromagnetic Interference Shielding with Ultrahigh Electromagnetic Wave Absorption. *Nano-Micro Lett.* **2025**, *17*, 291.

[S16] Li, Y. H.; Wang, Y.; Li, Z.; Ma, S. P.; Zhang, Y. W.; Fan, F.; Huang, Y. Meter-Scale Wearable Multifunctional Core-Shell Nanofiber Textiles for Ultra-Broadband Electromagnetic Interference Shielding and Infrared Stealth. *Adv. Mater.* **2025**, *37*, 2501485.

[S17] He, M.; Qian, W.; Li, H. Y.; Li, Z. H.; Chen, H.; Zhou, Y. M.; Bu, X. H.; Wang, Y. J. Ultrathin and flexible carbonized MXene@PAN/Ni films with alternating multilayered structure for superior EMI Shielding, Joule heating and mechanical performance. *Chem. Eng. J.* **2025**, *506*, 159777.

[S18] Yin, L.; Zhang, J. L.; Luo, J. J.; Shi, Y. Q.; Yu, B.; Zhang, S.; Zhou, K. Q. Janus-inspired alternating architecture CNF/MXene/$ZnFe_2O_4$@PANI composite films with outstanding electromagnetic interference shielding and Joule heating. *J. Mater. Sci. Technol.* **2025**, *223*, 275-286.

[S19] Liu, M. X.; Zhang, H. R.; Zhang, Z. Y.; Zhang, K. L.; Chen, Z. W.; Pan, L.; Zhou, J. T. Jujube-cake inspired lightweight and flexible MXene/liquid metal/bacterial cellulose electromagnetic interference shielding film with excellent Joule heating and thermal conductivity. *Compos. Sci. Technol.* **2024**, *255*, 110722.

[S20] Kim, J.; Choi, Y.; Jang, H.; Jiong, S.; Chen, X. Q.; Seo, B.; Choi, W. Thermo-Chemo-Mechanically Robust, Multifunctional MXene/PVA/PAA-Hanji Textile with Energy Harvesting, EMI Shielding, Flame-Retardant, and Joule Heating Capabilities. *Adv. Mater.* **2024**, *36*, 2411248.

[S21] Guo, Z. Z.; Ren, P. G.; Yang, F.; Wu, T.; Zhang, L. X.; Chen, Z. Y.; Ren, F. Robust multifunctional composite films with alternating multilayered architecture for highly efficient electromagnetic interference shielding, Joule heating and infrared stealth. *Compos. Pt. B-Eng.* **2023**, *263*, 110863.

[S22] Zhao, X.; Wang, L. Y.; Tang, C. Y.; Zha, X. J.; Liu, Y.; Su, B. H.; Ke, K.; Bao, R. Y.; Yang, M. B.; Yang, W. Smart $Ti_3C_2T_x$ MXene Fabric with Fast Humidity Response and Joule Heating for Healthcare and Medical Therapy Applications. *ACS Nano* **2020**, *14*, 8793-8805.

[S23] Cui, J. X.; Wu, J.; Feng, A. H.; Yu, Y.; Mi, L.; Yu, Y. Low infrared emissivity and oxidation stability of $Ti_3C_2T_x$ MXene-based composite with tannic acid. *Chem. Eng. J.* **2024**, *493*, 152289.

[S24] Zhu, H. Z.; Li, Q.; Zheng, C. Q.; Hong, Y.; Xu, Z. Q.; Wang, H.; Shen, W. D.; Kaur, S.; Ghosh, P.; Qiu, M. High-

Uncorrected

temperature infrared camouflage with efficient thermal management. *Light: Science & Applications* **2020**, *9*, 60.
[S25] Li, L.; Shi, M. K.; Liu, X. Y.; Jin, X. X.; Cao, Y. X.; Yang, Y. Y.; Wang, W. J.; Wang, J. F. Ultrathin Titanium Carbide (MXene) Films for High-Temperature Thermal Camouflage. *Adv. Funct. Mater.* **2021**, *31*, 2101381.
[S26] Shen, M. M.; Ni, J. H.; Cao, Y. X.; Yang, Y. Y.; Wang, W. J.; Wang, J. F. Low infrared emitter from $Ti_3C_2T_x$ MXene towards highly-efficient electric/solar and passive radiative heating. *J. Mater. Sci. Technol.* **2023**, *133*, 32-40.
[S27] Huo, Q. Q.; Liang, C. B.; Qi, J. M.; He, M. K.; Si, X. F.; Xue, F. P.; Qiu, H.; Gu, J. W. Bioinspired Asymmetric Janus Film Enables Concurrent Dynamic Infrared Camouflage and Electromagnetic Interference Shielding. *Adv. Funct. Mater.* **2026**, *36*, e22330.
[S28] Jin, X. X.; Wang, J. F.; Dai, L. Z.; Liu, X. Y.; Li, L.; Yang, Y. Y.; Cao, Y. X.; Wang, W. J.; Wu, H.; Guo, S. Y. Flame-retardant poly(vinyl alcohol)/MXene multilayered films with outstanding electromagnetic interference shielding and thermal conductive performances. *Chem. Eng. J.* **2020**, *380*, 122475.

Just Accepted